Chromosome Pairing Through Tensioned DNA Tethers Revealed by BRCA2 Meiotic Domain Deletion

Lieke Koornneef[1,2], Sari E. van Rossum-Fikkert[2,3], Esther Sleddens-Linkels[1], Simona Miron[4], Alex Maas[5], Yvette van Loon[2,3], Marco Barchi[6], Sophie Zinn-Justin[4], Jeroen Essers[2,7,8], Roland Kanaar[2,3*], Willy M. Baarends[1,*], Alex N. Zelensky[2,3*]

[1]*Department of Developmental Biology, Erasmus University Medical Center, 3000 CA, Rotterdam, The Netherlands*
[2]*Oncode Institute, Erasmus University Medical Center, 3000 CA, Rotterdam, The Netherlands*
[3]*Department of Molecular Genetics, Erasmus MC Cancer Institute, Erasmus University Medical Center, 3000 CA, Rotterdam, The Netherlands*
[4]*Institute for Integrative Biology of the Cell (I2BC), CEA, CNRS, Uni Paris-Sud, Uni Paris-Saclay, Gif-sur-Yvette, France*
[5]*Department of Cell Biology, Erasmus University Medical Center, 3000 CA, Rotterdam, The Netherlands*
[6]*Deparment of Biomedicine and Prevention, Faculty of Medicine, University of Rome Tor Vergata, Rome, Italy*
[7]*Department of Radiotherapy, Erasmus University Medical Center, 3000 CA Rotterdam, The Netherlands*
[8]*Department of Vascular Surgery, Erasmus University Medical Center, 3000 CA, Rotterdam, The Netherlands*

[*]Correspondence should be addressed to a.zelensky@erasmusmc.nl, w.baarends@erasmusmc.nl or r.kanaar@erasmusmc.nl

ABSTRACT

BRCA2 has multiple functional domains that interact with different partners, and is essential for both somatic and meiotic homologous recombination (HR). We created a *Brca2*$^{\Delta 12\text{-}14}$ mouse model with an internal deletion of the region which we named "the meiotic domain of BRCA2", as its loss results in complete failure of meiotic HR, while somatic HR is intact. The deletion in the protein includes the HSF2BP-binding motifs (exons 12-13) and the DMC1-binding PhePP domain (exon 14). *Brca2*$^{\Delta 12\text{-}14}$ mice showed complete infertility in both males and females, with sexually dimorphic features. Recombinase foci (both RAD51 and DMC1) were completely undetectable in mutant spermatocytes, but while DMC1 foci were also absent in mutant oocytes, RAD51 foci numbers were only partially reduced (up to 60% fewer, 20% less intense). The relevance of the PhePP domain for meiotic HR has been controversial, but both the phenotype of *Brca2*$^{\Delta 12\text{-}14}$, and our biochemical data indicate that, along with the BRC repeats of BRCA2, PhePP is both essential and specific for DMC1 loading in meiotic HR, analogous to the C-terminal RAD51-specific TR2/CTRB. Further investigation of DSB end processing in *Brca2*$^{\Delta 12\text{-}14}$ meiocytes and controls, using super-resolution imaging of RPA and SYCP3 led to discovery of two novel features. First, in *Brca2*$^{\Delta 12\text{-}14}$ oocytes, but not in the spermatocytes nor wild types, we observed RPA foci as doublets ~200 nm apart, which could represent DSB end separation. Second, we describe RPA structures that are completely HR-dependent and are indicative of long, double-stranded DNA connections between homologs prior to synapsis. The observations led us to a model for chromosome alignment via multiple, tensed DNA tethers that connect the homologous DNA regions. We propose that in combination with dynamic adjustment of chromatin loops by meiotic cohesins, this is a plausible molecular mechanism to bring the homologs closer and initiate synapsis.

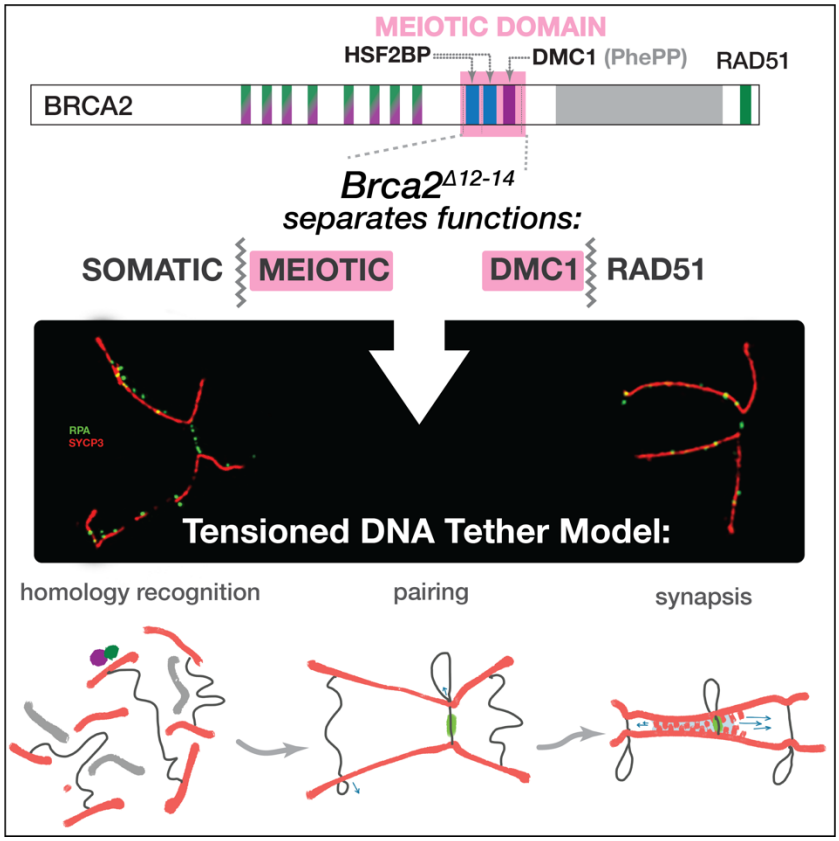

INTRODUCTION

BRCA2 is essential for both mitotic and meiotic homologous recombination (HR) in vertebrates [1,2]. Its meiotic role is evolutionarily ancestral: loss of fertility due to meiotic HR failure is the universal and the most pronounced phenotype resulting from the deletion of BRCA2 orthologues in fungi[3], plants[4,5], protozoa[6] and invertebrates[7–10]. However, few details are available about the exact meiotic function of BRCA2. There is no BRCA2 orthologue in budding yeast, a key model system for mechanistic studies of meiosis. Also, in vertebrates, studies of BRCA2 in meiosis are limited by embryonic lethality of *Brca2* knockout in mouse and difficulty of immunodetection of the protein on meiotic chromosome spreads. Thus, the mechanistic understanding of BRCA2 in meiosis is mostly based on inferences from the studies of mitotic HR and limited biochemical experiments. Still, three mouse models confirmed the critical role of *Brca2* in mouse meiotic HR: a knockout rescued by a hypomorphic transgene that is not active in meiocytes[11] and two mouse strains with different truncating mutations in exon 11 [12,13]. In all cases complete infertility of both sexes was observed. While BRCA2-mediated loading of RAD51 in somatic cells is required for repair of accidental DNA damage, loading of RAD51 and its meiosis-specific paralog DMC1 in meiosis is essential for the repair of programmed DNA double-strand breaks (DSBs). This special form of HR repair is then pivotal to achieve complete and stable homologous chromosome pairing and synapsis (formation of the synaptonemal complex connecting the homologous chromosomes), as well as for crossover formation.

Studies on BRCA2 in somatic cells were focused on its functional interaction with RAD51, the recombinase that performs homology recognition and strand exchange during HR. BRCA2 also interacts with DMC1 [14–17], the meiosis-specific paralog of RAD51. The BRCA2 BRC repeats encoded by *BRCA2* exon 11 interact with both recombinases, and there are additional sites that interact with only one: the RAD51-binding site in the C-terminal domain of BRCA2 encoded by exon 27, and the DMC1-binding site located before the highly conserved DNA-binding domain and encoded by exon 14 [16]. The data on this DMC1-specific interaction domain is contradictory: it was identified biochemically using recombinant proteins [16], but its physiological relevance was later put into question when a mouse strain with a nonconservative substitution of phenylalanine 2351 to aspartate in BRCA2 was engineered [18]. The mouse F2351 corresponds to F2406 in human BRCA2, which was absolutely essential for the interaction between recombinant human BRCA2 and DMC1 *in vitro*. However, the *Brca2*^{F2351D} mice were fully fertile.

We and others have recently discovered that BRCA2 forms a high-affinity complex with the previously uncharacterized protein HSF2BP (also called MEILB2) in mouse embryonic stem (mES) cells and meiocytes [19–24]. Mice deficient for HSF2BP are born at Mendelian ratios and have no overt somatic phenotypes, but males are infertile due to meiotic HR failure. Shortly after, HSF2BP was shown to directly interact with another uncharacterized protein named BRME1 (also called MAMERR or MEIOK21), and the phenotypes of the *Hsf2bp* and *Brme1* knockout mouse models[19,21,25–29] were similar.

To test whether HSF2BP interaction with BRCA2 is crucial for its meiotic function, we previously generated and characterized a mouse strain lacking *Brca2* exon 12 [22], which encodes one of the two motifs comprising the HSF2BP-binding domain (HBD, Figure 1A) of BRCA2, the other motif is localized in exon 13. As exon 12 boundaries fall in the same position relative to the reading frame, this deletion did not lead to a frame shift. The *Brca2*$^{\Delta 12}$ mice were phenotypically normal and fertile, in contrast to the male sterility of the *Hsf2bp* knockout [19,21,25]. This put the role of HSF2BP-BRCA2 interaction in meiotic HR into question. However, while exon 12 deletion reduced HSF2BP-BRCA2 interaction, it did not completely abolish it *in vivo*. The residual affinity was higher in the testis co-immunoprecipitation experiments than in

biochemical experiments with purified or ectopically produced proteins, suggesting that additional factors may contribute to the HSF2BP-BRCA2 interaction in the physiological context. In the same work, we also characterized mES cells with a deletion of exons 12 through 14 of *Brca2* (Δ12-14). Exon 14 is the nearest downstream exon that can be co-excised with exon 12 while preserving the reading frame. In addition to the two HSF2BP-binding motifs encoded by exons 12 and 13, deletion of exon 14 removes a block of conserved amino acids that includes the site that has previously been shown to bind to DMC1 (the PhePP motif [16]), as mentioned above. In these cells HSF2BP did not co-precipitate at all with the BRCA2 produced from the deletion allele.

Here we describe the phenotype of the mouse model with *Brca2* exon 12-14 deletion, which lacks both HSF2BP-binding domains and the purported DMC1-binding site. The strain is viable but completely infertile, thus defining the deleted region as the "meiotic domain" of BRCA2. The phenotype provides novel insights into BRCA2 structure-function relationships in terms of somatic versus meiotic functions, and male versus female functions. In addition, the complete lack of recombinase loading in the male mutant spermatocytes revealed that RPA-bound tensioned DNA tethers between homologs form downstream of recombinase loading, and our super-resolution analyses led us to propose a model that postulates a role for tensioned DNA tethers in homologous chromosome pairing and synapsis.

RESULTS

No somatic defects and complete meiotic arrest in Brca2$^{\Delta 12\text{-}14}$ mouse

To test whether the complete removal of the BRCA2 HSF2BP-binding domain recapitulates the *Hsf2bp* knockout phenotype, we engineered a homozygous mouse strain lacking *Brca2* exons 12-14 (*Brca2$^{\Delta 12\text{-}14}$*), following the strategy we previously tested in mES cells [22] (Figure 1A-C). Consistent with the lack of HR defects in mES cells carrying the same mutation (Figure S1 and ref [22]), *Brca2$^{\Delta 12\text{-}14}$* mice were viable, of normal appearance, and were born at Mendelian ratios (Figure 1D). However, *Brca2$^{\Delta 12\text{-}14}$* males as well as *Brca2$^{\Delta 12\text{-}14}$* females were infertile, demonstrated by the lack of successful breedings after mating 8 *Brca2$^{\Delta 12\text{-}14}$* males and 6 *Brca2$^{\Delta 12\text{-}14}$* females with their corresponding wild type partners. In males, *Brca2$^{\Delta 12\text{-}14}$* testes were smaller (Figure 1E) with 70% reduced weight compared to wild type (Figure 1F). Epididymis weight was also reduced by 54%, whereas body weight was unaffected (Figure 1G-H). Histological analyses of *Brca2$^{\Delta 12\text{-}14}$* testes showed that development of germ cells did not proceed beyond the spermatocyte stage (Figure S2A). In adult females we observed a reduction in size of the internal reproductive organs (Figure 1I). Histology of adult ovaries showed absence of follicles (Figure S2B). Together, this shows that exons 12-14 of *Brca2* are essential for fertility in both male and female mice.

Synapsis in Brca2$^{\Delta 12\text{-}14}$spermatocytes is aberrant but more extensive compared to that of Spo11 knockout

Next, we studied the cause of *Brca2$^{\Delta 12\text{-}14}$* mice infertility using immunofluorescent staining for meiotic prophase proteins on *Brca2$^{\Delta 12\text{-}14}$* meiocyte spread nuclei and corresponding wild type littermate controls, which revealed major defects. Starting with staining for axial/lateral filaments of the synaptonemal complex (SYCP2 or SYCP3), we observed that *Brca2$^{\Delta 12\text{-}14}$* spermatocytes initiate synapsis, but fail to perform it faithfully, resulting in a late zygotene-like appearance of the most advanced cell types (Figure S3A,B). In regions where synapsis occurred, SYCP1 (which forms the transverse filaments of the SC) was present, as expected (Figure S3C). Similar observations were made in E17.5 *Brca2$^{\Delta 12\text{-}14}$* oocytes (Figure S3D,E).

To investigate synapsis progression in spermatocytes in more detail, we used structured illumination microscopy (SIM) to study SYCP3. First, we observed that 91% of the partially synapsed regions in the mutant included telomeric ends, while this was only 66% for wild type, where partial synapsis was more often observed only in a central region, excluding the telomeres ($p < 0.001$, unpaired two-sided t-test, fully synapsed chromosomes were excluded) (Figure S3F,G). Second, we observed that within the *Brca2$^{\Delta 12\text{-}14}$* spermatocytes most synapsis was non-homologous, as it often involved multiple chromosomes, but also apparently completely synapsed configurations were clearly detected (Figure S3H). The frequency of these fully synapsed chromosome pairs (average of four fully synapsed configurations per nucleus) was two times higher in our *Brca2$^{\Delta 12\text{-}14}$* model than in a model without DSB formation (*Spo11$^{-/-}$* mutant) (Figure S3I). Third, we assessed whether this complete end-to-end synapsis was homologous by performing fluorescent in situ hybridization (FISH) of chromosome 13 in combination with immunocytochemistry of SYCP3, and determined the number of FISH clouds per nucleus and the degree of synapsis at the position of the cloud(s) (Figure S3J). Of the 121 nuclei in which one or two FISH signals were detected, only 9 (7.4%) displayed a single cloud on a fully synapsed chromosome (Figure S3K), as would be expected for homologous synapsis, while in 43 (36%) there was also a second cloud elsewhere, as expected if chromosome 13 was engaged in nonhomologous synapsis. Furthermore, the

7.4% is an overestimate of homologous synapsis, as single cloud observation may also result from non-detection of the second chromosome for technical reasons, as evidenced by 11 nuclei (9.1%) displaying a single cloud on unsynapsed regions or regions with aberrant synapsis involving more than two lateral elements or lateral elements of unequal lengths. Together, this shows that in absence of exon 12-14 of *Brca2*, homologous chromosome synapsis is abrogated, but non-homologous synapsis still occurs, more often initiating at telomeres compared to homologous synapsis, and more often than in the absence of DSB formation.

Brca2$^{\Delta 12\text{-}14}$ differentially affects DMC1 and RAD51 in oocytes and spermatocytes

As homologous chromosome synapsis is dependent on HR [11,30–33], and BRCA2 acts as HR mediator, we next analyzed the localization of RAD51 and DMC1 recombinases in spermatocyte and oocyte nuclei. In *Brca2$^{\Delta 12\text{-}14}$* spermatocytes, both RAD51 and DMC1 foci were completely absent (Figure 2A-C). To exclude defects in DSB formation, we assessed loading of the single-stranded DNA binding protein RPA as marker for DSB formation. In the mutant, RPA foci were present and the number was increased compared to wild type (Figure 2D,E), suggesting that DSBs can be formed, but that RPA cannot be replaced by recombinases. Also, the foci numbers of SPATA22, a meiosis-specific single-stranded DNA binding protein [34–36], were higher in absence of exons 12-14 of *Brca2* than in the controls (Figure 2D,F), similar to what was observed in *Hsf2bp$^{-/-}$ and Brme1$^{-/-}$* spermatocytes [19,25,27,28]. Since the *Brca2$^{\Delta 12\text{-}14}$* mouse model completely lacks the HSF2BP-binding domain, we investigated the localization patterns of HSF2BP and its interaction partner BRME1. Both proteins were present in foci but behaved differently in the mutant (Figure 2G). HSF2BP foci numbers were reduced, while BRME1 foci numbers were increased (Figure 2H,I). Moreover, the intensity of the RPA, BRME1 and SPATA22 foci was increased (Figure S4A), while the intensity of HSF2BP was unaffected in *Brca2$^{\Delta 12\text{-}14}$* spermatocytes (Figure S4B).

Hsf2bp$^{-/-}$ and *Brme1$^{-/-}$* mice showed a sexual dimorphism regarding defects in meiosis [19,21,25–29,37]. Therefore, we also analyzed meiotic HR protein localization patterns in embryonic (E15.5 and E17.5) *Brca2$^{\Delta 12\text{-}14}$* oocyte nuclei, since female meiotic prophase initiates during embryogenesis. Similar to the male mutant, DMC1 foci were not observed (Figure 3A,B). However, RAD51 foci were detected (Figure 3A), but their number in leptotene-like nuclei was 60% lower than in wild type leptotene (Figure 3C) and the foci were 20% less intense (Figure S4C). RAD51 foci numbers remained constant between early zygotene and late zygotene (Figure S4D), which distinguishes this mutant from *Hsf2bp$^{-/-}$* oocytes where, despite similar initial RAD51 foci numbers as in *Brca2$^{\Delta 12\text{-}14}$* oocytes, RAD51 foci numbers decreased as cells progressed during meiotic prophase [25] (Figure S4D). This could imply that meiotic HR repair progresses to a point where RAD51 protein is removed in *Hsf2bp$^{-/-}$* oocytes, but not in *Brca2$^{\Delta 12\text{-}14}$* oocytes. In addition, and similar and consistent with *Brca2$^{\Delta 12\text{-}14}$* males, RPA foci were present in *Brca2$^{\Delta 12\text{-}14}$* oocytes and numbers were increased (Figure 3D,E), confirming formation of DSBs. Also, SPATA22 foci numbers were increased in absence of exons 12-14 of *Brca2* (Figure 3D,F). Like SPATA22, HSF2BP and BRME1 showed the same changes as observed in the mutant spermatocytes: reduced HSF2BP, and increased BRME1 foci numbers (Figure 3G-I). Furthermore, the HSF2BP intensity was reduced, while the RPA, BRME1 and SPATA22 foci intensity was increased in the mutant oocytes (Figure S4E,F).

DMC1-binding PhePP domain in exon 14 of Brca2

The meiotic phenotype of *Brca2$^{\Delta 12\text{-}14}$* was clearly distinct from that of *Hsf2bp* knockout. It was more severe, and in the females involved complete loss of DMC1 but not of RAD51 recombinase accumulation.

This latter observation strongly suggested that the deleted region contains, in addition to the HSF2BP-binding domain, a domain that specifically affects DMC1 function. A previous publication [16] suggested that BRCA2 exon 14 encodes a direct BRCA2-DMC1 interaction domain involving the PhePP motif, however, this was not validated in any follow-up biochemical studies, and a specific mutant mouse model testing it revealed no effect on meiosis [18]. We therefore proceeded to replicate and extend the previously published observation using recombinant DMC1 and BRCA2 fragments expressed in *E. coli* (Figure 4, S5).

DMC1 co-precipitated with the GST-tagged BRCA2 fragment F6, corresponding to the region deleted in our mouse model, and with F2, corresponding to exon 14, but not with F8 corresponding to exons 12-13, and F2406A substitution within the PhePP motif completely abolished this interaction (Figure 4A,B). Using a truncation fragment series we narrowed down the interaction domain to BRCA2 residues 2379-2433, fragment F2s3. Purified F2s3, but not its F2406A variant co-precipitated with purified DMC1 but not with RAD51, further demonstrating that the interaction is direct (Figure 4C,D, S5C). We used isothermal titration calorimetry (ITC) to determine that the small synthetic peptide F2s6, corresponding to the conserved region of F2s3, still bound to the purified untagged DMC1 with a Kd of 3.4 µM, and no interaction was observed when the same assay was performed with the F2406A mutant. In addition, testing a similar motif encoded by exon 27, in the so-called TR2 region, revealed that despite the presence of a similar (FQPP) motif, that was shown to bind RAD51 [38], this fragment does not interact with DMC1 (Figure 4E, S5D). Taken together, these results confirm the presence of a specific DMC1-interacting motif in the region encoded by exon 14 of BRCA2.

Distinct RPA foci patterns in Brca2$^{\Delta 12\text{-}14}$ versus wild type zygotene meiocytes

The *Brca2*$^{\Delta 12\text{-}14}$ mouse model provides opportunities for studying the initial steps of meiotic DSB repair, due to the complete lack of recombinase loading in spermatocytes. In particular, in this mutant initial RPA loading on single-stranded (ss)DNA should still occur (RPA on resected ends; RPA-R), while possible RPA loading on ssDNA in the D-loop (RPA-D) would be expected to be abrogated in the absence of recombinases. Thus, comparing RPA localization patterns between wild type and *Brca2*$^{\Delta 12\text{-}14}$ meiocytes might provide insight in which localization patterns are specific for the initial RPA loading on resected ssDNA. We used the super-resolution microscopy technique SIM to visualize RPA localization in *Brca2*$^{\Delta 12\text{-}14}$ and control spermatocytes and oocytes (Figure 5A-B). First, we investigated the position of RPA foci relative to the axial and lateral elements of the SC by measuring the shortest distance from each focus to the axial elements (unsynapsed regions) or to the center of two lateral elements (synapsed regions) (Figure 5C-E). Quantification showed that the distance of RPA foci to the axial or central elements in *Brca2*$^{\Delta 12\text{-}14}$ zygotene spermatocytes was significantly larger than in wild type spermatocytes. This difference was not observed for *Brca2*$^{\Delta 12\text{-}14}$ oocytes.

Second, we also quantified the number of RPA foci in the super-resolution images (Figure 5F). In *Brca2*$^{\Delta 12\text{-}14}$ oocytes, we quantified a median of 558 RPA foci within a nucleus, compared to 357 in wild type oocytes ($p<0.0001$). In *Brca2*$^{\Delta 12\text{-}14}$ spermatocytes fewer RPA foci were observed (421), which was still more than in wild type spermatocytes (351, $p<0.003$). This increase in both male and female mutants is consistent with our observations using confocal microscopy (Figure 2E, 3E), but the numbers of detectable RPA foci are higher using SIM than using confocal microscopy. This indicates that several RPA foci were closer than the resolution limit in the confocal images, especially in *Brca2*$^{\Delta 12\text{-}14}$ oocytes. Indeed, in the SIM images of mutant oocytes we observed a distinct RPA positioning pattern at unsynapsed regions, with often two RPA foci positioned closely together as a doublet (Figure 5G,H). These RPA

doublets were much less apparent in wild type oocytes or in wild type and *Brca2*$^{\Delta 12\text{-}14}$ spermatocytes. To further analyze these doublets, we determined the nearest neighbor distance for all RPA foci, and indeed observed an almost doubled density frequency for a distance of ~200 nm in *Brca2*$^{\Delta 12\text{-}14}$ oocytes compared to controls (Figure 5I,J), while the RPA nearest neighbor distance distribution patterns of wild type oocytes and spermatocytes, as well as of *Brca2*$^{\Delta 12\text{-}14}$ spermatocytes were all very similar, with a peak at around 350 nm (387 nm for wild type oocytes, 352 nm for wild type spermatocytes, and 318 nm for *Brca2*$^{\Delta 12\text{-}14}$ spermatocytes).

A third remarkable feature of RPA localization that is particularly clear in the SIM images is the presence of the class of foci we named "RPA tethers". They are exclusively present in the wild type and appear either as highly elongated individual foci or linear constellations of circular foci along an invisible line that appears to be connecting two chromosomal axes. Several different tethers in different structural contexts are shown in Figure 6A. They become detectable in leptotene between fragments of axial element that are distinctly kinked giving an impression of the connection. During the progression through zygotene the tethers appear between continuous axial elements that do not (yet) display any form of parallel alignment, and become more numerous in the context of partially aligned as well as partially synapsed chromosome pairs in zygotene. When kinks are present on both axes in a symmetric orientation, they create a "butterfly" appearance (Figure 6A structures #2-5, and Figure S6C). The tethers that we observed between partially synapsed and aligned segments of chromosomes are similar to RPA structures reported previously by others, and often termed bridges[39–41]. No tethers were observed in the *Brca2*$^{\Delta 12\text{-}14}$ spermatocytes (16 nuclei, 2 animals), which shows that their formation depends on recombinase loading. We quantified all tethers, noting the presence or absence of kinks and their chromosomal context in terms of alignment and/or synapsis (Figure 6B,C). Of 81 wild type nuclei analyzed from 4 animals in two experiments, we observed 474 tethers. The majority (90%) of tethers in a context without parallel alignment (early structure, n=91) displayed kinks. As alignment became apparent, the frequency of kinks reduced to 39% (mid structure, n=197), and in a context of partial synapsis, this percentage was similar (late structure, 35% kinks, n=185, Figure 6C). Moreover, the length between the kinks (or the attachment point on the chromosomal axes of the invisible tether if kinks were not present) decreased as meiotic prophase progressed (Figure 6D). Also, the distance was larger when kinks were present (no kinks: 0.55±0.29 µm, kinks: 0.86±0.41 µm). We noted that in thirteen examples of the fully traceable butterfly configuration we found, axial elements were arranged symmetrically, with longer parts on the same side of the tether (examples #2-#5 in Figure 6A and 9 structures in Figure S6B (#3) and S6C #1,2,3,4,5,9,13,15) indicating that for these connections, the chromosomal axes were orientated in accordance with the expected homology. This resembles the "pinched" configuration of zebrafish chromosomes initiating synapsis [42]. Conversely, we also observed two occasion(s) where the orientation appeared reversed (Figure S6C #7 and S7D #2). It should be noted that multiple RPA tethers were not often observed in the context of early chromosomal arrangements (19 out of 91 early arrangements had multiple tethers) but present in the majority of mid and late chromosomal arrangements. To corroborate our findings, we performed a similar analysis on wild type slides using SPATA22 and BRME1 antibodies, since these two proteins have been reported to colocalize with RPA [25,26,28,43]. Indeed, similar tethers were observed with both antibodies (Figure S7). Together, these findings point towards the hypothesis that RPA tethers and their chromosomal arrangements are HR-specific chromosome connections and contribute to homologous chromosome pairing and synapsis.

DISCUSSION

The meiotic domain of Brca2

We generated and characterized a mouse strain that separates the meiotic functions of BRCA2 from its essential role in somatic HR, that allowed detailed functional analyses. Deletion of *Brca2* exon 12 to 14 resulted in a complete block of meiotic HR and infertility in both sexes, consistent with reported *Brca2* hypomorphic mouse models [11,12] and BRCA2 mutants in other species [3–10]. As no developmental or other somatic defects were detectable, we propose that the deleted region constitutes the "meiotic domain" of BRCA2, and that variants of unknown significance within it are unlikely to be cancer-associated [44,45]. It contains two previously described meiosis-related regions: the HSF2BP-binding repeated motif encoded by exons 12 and 13, and the DMC1-binding PhePP domain encoded by exon 14. Characterization of the latter is particularly significant, as published data had been conflicting [16,18]. Its functional relevance is now supported by the cytological (complete loss of DMC1 foci but partial retention of RAD51 foci, Figures 2-3) and biochemical (details of direct interaction between PhePP and DMC1, Figure 4) data. Our findings suggest that the FxPP consensus does not fully capture the recombinase binding requirements, as PhePP binds DMC1 and not RAD51, while the RAD51-binding "TR2" motif [38] encoded by exon 27 does not bind DMC1, despite similar core sequence (FVPP and FQPP, respectively). BRCA2 thus binds both RAD51 and DMC1 via two distinct domains: the BRC repeats, which bind monomeric forms [46] of both recombinases, and additional FxPP motifs that are recombinase-specific. We further explore the hypothetical functional analogy between PhePP-DMC1 and TR2-RAD51 interactions in a separate study, which describes the crystallographic structure of the complex between DMC1 and BRCA2 PhePP fragment and provides additional molecular and functional detail on this interaction [47].

Sexual dimorphism in RAD51 loading

The meiotic phenotype of *Brca2*$^{\Delta 12\text{-}14}$ is more severe than that of *Hsf2bp*$^{-/-}$. Since both HSF2BP- and DMC1-binding domains were deleted, it may be a compound phenocopy of the two respective phenotypes: the sexually dimorphic phenotype of the *Hsf2bp* knockout (greatly reduced RAD51 and DMC1 foci in the male, but both form in females) [18,20,24] combined with a non-dimorphic *Dmc1* knockout phenotype (RAD51 foci still form in both sexes, DMC1 lost) [32,33]. However, RAD51 (and DMC1) foci are not completely ablated in *Hsf2bp*$^{-/-}$ spermatocytes [21,25]. In addition, the striking persistence of RAD51 foci numbers in late zygotene oocytes of *Brca2*$^{\Delta 12\text{-}14}$ animals highlights a sexual dimorphism in RAD51 loading. These and other interpretations and their possible limitations are addressed in the Extended Discussion.

DSB formation stimulates synapsis

We observed more complete end-to-end synapsis in *Brca2*$^{\Delta 12\text{-}14}$ than in *Spo11* knockout spermatocytes (Figure S3I). Still, these represented non-homologously synapsed chromosomes. In the absence of recombinase loading, this indicates that DSB induction and end resection somehow stimulate non-homologous synapsis. Synaptic adjustment mechanisms, similar to what is often observed in mice carrying regions of non-homology due to translocations, duplications, or inversions [48,49], could further contribute to establishing complete end-to-end pairing. We note that partially synapsed chromosome pairs in *Brca2*$^{\Delta 12\text{-}14}$ spermatocytes always have synapsed telomeres (Figure S3F,G), while a third of wild type chromosomes do not, and hypothesize that non-homologous synapsis initiates at telomeres, while homologous synapsis can begin interstitially.

High-resolution analysis of RPA in females showed a preferred doublet formation

Complete block of HR steps downstream of RAD51/DMC1 nucleoprotein filament formation allowed us to address some long-standing questions regarding the role of ssDNA-binding proteins, which are thought to accumulate on ssDNA after end resection (forming RPA-R foci) as well as on ssDNA formed in a post-strand-invasion context (D-loop, forming RPA-D foci). Morphological differences between those two types remain unknown. We hypothesized that RPA-D foci would be absent in our HR-deficient mutant, allowing assessment of RPA-R foci only. Previously, it has been suggested that RPA foci in between synapsed regions represent post-invasion structure, while pre-invasion RPA would be present on axial elements, or along the outer edge of the SC [39–41,50]. Consistently, we observed a larger distance of RPA foci to the axial/lateral elements of the SC in *Brca2*$^{\Delta 12\text{-}14}$ spermatocytes compared to controls. Although there is an expected loss of RPA-D foci, we still observed an increase in RPA foci numbers in the mutant. This is most likely at least in part due to continued DSB formation in the absence of repair and homologous chromosome synapsis. However, the number of detected foci may also depend on whether one or both DSB ends are RPA loaded and whether these ends are separated at discernible distances. Intriguingly, only in the *Brca2*$^{\Delta 12\text{-}14}$ oocytes we observe formation of distinct RPA doublets with a preferred distance of ~200 nm (Figure 5J), along with a more pronounced increase in RPA foci number than in *Brca2*$^{\Delta 12\text{-}14}$ spermatocytes, that do not display an altered pattern of foci distribution (Figure 5F). The simplest interpretation is that these RPA doublets represent the two ends of a DSB, both loaded with RPA, that became separated. We do not exclude that such doublets also occur in the males, and also in wild type meiocytes, as might be inferred from visual inspection. However, the quantitative analyses that we performed indicates that these instances may be random events, or too rare to be detected as a prominent peak in the nearest neighbor analyses. The mechanism underlying occurrence of more frequent RPA doublet formation only in *Brca2*$^{\Delta 12\text{-}14}$ oocytes could be related to the partial retention of RAD51 function in oocytes or could involve more general mechanistic differences in meiotic HR between sexes [51]. The peak of ~ 200 nm in the distance distribution could reflect the structural properties of RAD50 or other end-tethering components [52,53]. An alternative, but in our view less likely explanation is that the doublets are the result of exactly two DSBs in close, and more or less fixed proximity, either on the same chromatid or on the sister, like the recently described double-DSBs [54,55].

The tensioned DNA tether model of homologous synapsis

Brca2$^{\Delta 12\text{-}14}$ spermatocytes showed a complete lack of the RPA foci class we called "tethers" (Figure 6A-C), observed between homologs as they progress towards synapsis. RPA foci in late structures, in association with clear parallel alignment, have been documented previously in mice and humans [39–41,50]. In addition, similar connecting structures have also been reported in plants and fungi [56–59]. In the fungus *Sordaria macrospora*, these structural arrangements have been termed "bridges" and displayed enrichment of the so-called ZMM proteins (components of the synaptonemal complex, Mer3, and MSH4), when the distance of coaligned chromosomal axes transitions from a 400 nm to 200 nm or less [58,59]. However, the earlier and much rarer structures at larger distances (~1 µm and as long as 12 µm, Figure S6B #2) that we report here have eluded attention (see the "pinch" configuration in ref. [42]). These recombinase-dependent tethers, along with the associated chromosomal structures, have led us to the "tensioned DNA tether" model of homologous synapsis (Figure 7, S8, Supplementary Movie). Our model originates from the interpretation of the three key morphological features that are most obvious in the distinct "butterfly" chromosome configuration (Figure 6A, S6A, C, S8A,B). Their first key feature is the shape and arrangement of the RPA tether foci, which follow a straight line projecting towards the axial elements. The second are distinct kinks in the axial element towards which the line projects. The kinks are most

pronounced in the early stages (Figure 6), but are also observed in part of the late synapsed structures (examples #7, #9 in Figure 6A) and were previously noted there as "inflections" by Moens *et al.* [41]. Together, the kinks and the shape of the RPA foci suggest that the chromosomes are connected by tensioned DNA that contains one or more ssDNA regions covered with RPA (Figure 7, S8A,B). Notably, tensioned dsDNA is known to melt and bind RPA *in vitro* [60,61] and *in vivo* in ultrafine anaphase bridges [62], suggesting an explanation of RPA localization in addition to the two (RPA-R and RPA-D) discussed above. The third key feature is the general symmetry of the butterfly arrangement: when the RPA tether is positioned eccentrically, the lengths of axial elements on both sides of it are equal. To explain this symmetry, we hypothesize that in addition to the tether that is tensioned and thus recognizable via RPA staining, multiple additional DNA tethers per pair of homologs are present (Figure 7B, S8B). They are not tensioned but provide the constrains that establish the correct end-to-end presynaptic juxtaposition. The second concept that we introduce is that we hypothesize that the DNA tether length is adjustable by molecular motors associated with it (Figure S8B). Both inferences are supported by the observation that tethers become shorter and more numerous as the homologs progress towards synapsis (Figure 6B-D). Shortening of the DNA tether, e.g. by reeling in of a chromatin loop as suggested previously [63–66] , would move the homologues close together to a distance short enough for proteinaceous bridges and SC to form[58,67] (Figure S8C,E,F). If the movement encounters sufficient resistance from clashes and entanglements with other structures, tension can result in axial element kinking and sometimes even in dsDNA melting (Figure S8D,F). Telomere movement could also be a tensioning force, but it alone does not explain the observed tether shortening.

The model outlined above not only explains well the genesis of the RPA tethers we described and the associated chromosome structures, but also suggests straightforward explanations for the otherwise mysterious events leading to homologous chromosome synapsis (Figure S8E-G). While somewhat similar ideas have previously been expressed to explain presynaptic events in *S. cerevisiae* and *Sordaria* [63–66], the deduction of tensed RPA-bound DNA, tethering homologs prior to synapsis, led us to additional crucial inferences. In retrospect, the idea that homologs need to be held and pulled together by DNA tethers before synapsis seems so unavoidable that it could be postulated without our experimental observations. As we describe below, illustrate in the Supplementary Movie, Figure S8E,F and elaborate in the Extended Discussion, this is because tensioned DNA tethers can fill two gaps in the current models of chromosome pairing in mammals.

The first gap is temporal: recombinase loading and HR are initiated in leptotene, while synapsis and establishment of end-to-end alignment that precedes it require continuous axial elements and happen in zygotene. Maintaining the precious homologous contacts that are most likely established before alignment initiates (based on tethers between kinked axial elements) would require robust flexible connections that can survive the dynamic rearrangements of the early prophase: assembly of the axes, bouquet formation, telomere motions etc. The formation of adjustable DNA tethers already in leptotene, as inferred from the current RPA staining results, are very suitable candidates for fulfilling this function.

The notion of the second, spatial, gap is perhaps less trivial and is not specifically considered in current theoretical modeling approaches [68,69]. This spatial gap represents the actual distance between the axial elements, and how it can be reduced to allow synapsis initiation (Figure S8D). In addition, synapsis may initiate non-homologously from persistent random collisions between axial elements, as it happens at telomeres in *Brca2*$^{\Delta 12\text{-}14}$. Thus, a mechanism is required to communicate that the two regions of the axes that came into proximity are bona fide anchor points of homologously interacting DNA molecules rather

than a much more probable random collision. Based on the localization of the vast majority of recombinase foci in close association with the axial elements in mouse spermatocytes and oocytes (first described by the group of Peter Moens [40,41,70]), even in super-resolution images [71,72], we postulate that both ends of a meiotic DSB remain within ~250 nm of the axial element of the chromosome. However, the homologous DNA repair template donor molecules for meiotic HR are not (yet) anchored in the axial element: this sequence will be located in a large chromatin loop, and thus, even upon homology recognition and stable strand invasion, the two homologous axial elements would still be far away from each other [59,73]. However, synapsis initiation requires a much closer proximity than the length of chromatin loops, our conservative estimate is <400 nm vs >>1000 nm. Reeling in of the DNA tether is a straightforward solution to bridging this spatial gap, and establish prolonged close proximity of the homologous axial elements. This would allow a distinction between two approaching homologous axial elements and the above-described frequent random collisions of heterologous axial elements, that would be short(er)-lived. The associated tension that goes along with reeling in of the tether may also serve as a signal. This process will then position the HR intermediate between the lateral elements, where it is detected after synapsis.

The general definition of the model presented above is compatible with several molecular scenarios, detailing the origin of tether-associated RPA, the nature and location of the tension-inducing motor, timing of HR events and configuration of DSB ends (see table in Extended Discussion). As detailed in the Extended Discussion, we consider meiotic cohesins, the most attractive candidate for performing the motor role (Figure S8C). Intriguingly, one of the consequences of *Rec8* knock-out in mouse is distant alignment of pairs of equally-sized chromosomes [74], which is the phenotype expected if both tether shortening and non-homologous synapsis were blocked. Furthermore, postulating the presence of active molecular motors reeling chromatin loops in and out, resulting in dynamic, regulated, adjustable structures, provide straightforward explanations for several events that require directional movement of DNA, such as translocation of the DSB hotspot to the axial element, (re)-unification of (separated) DSB ends in the asymmetric ("tentacle") model of DSB processing and homology search [59,73], and the assembly of continuous axial elements (Figure S8E). This flexibility, and possible redundancies, make straightforward genetic testing of the model challenging. In this regard, identification of the molecular motor activities responsible for shortening the length of the DNA tethers would be pivotal. In the Extended Discussion we consider several candidates for the motor role. Besides that, creation of new mouse models, including models to further delineate the BRCA2 meiotic domain, will be required to determine if the vast explanatory power of this speculative model is experimentally verifiable, and which of the proposed molecular scenarios are at play.

METHODS

Animals

Brca2$^{\Delta 12\text{-}14}$ mice were generated by two CRISPR/Cas9 cut excision, as described before [21,22]. Female donor mice (age 5 weeks, C57BL/6 OlaHsd from Envigo) were superovulated by injecting 5-7.5 IE folligonan (100-150 µl, IP (FSH hormone; time of injection ± 13.30 h; day -3). Followed at day -1 by an injection of 5-7.5 IE chorulon (100-150 µl, IP (hCG hormone; time of injection 12.00 h). Immediately after the chorulon injection, the females were put with fertile males in a one to one ratio. Next day (day 0), females were euthanized by cervical dislocation. Oviducts were isolated, oocytes collected and injected with ribonucleoprotein complexes of S.p.Cas9 3NLS (IDT cat. no. 1074181), crRNA and tracrRNA (both with Alt-R modifications, synthesized by IDT). Target sequences for crRNA were TAATATTCCAACCCTCGTGT (*Brca2* intron 11) and TGAGGCTTCCCTTAGGATTG (*Brca2* intron 14). For ribonucleoprotein formation equal volumes (5 µL) of crRNA and tracrRNA (both 100 µM in IDT annealing buffer) were mixed, heated to 95 °C for 5 min and allowed to cool on the bench and frozen. Two injections were performed. On the day of injection, the annealed RNAs (1.2 µL, 50 µM) were thawed, mixed with Cas9 (10 µl diluted to 200 ng/µl in the DNA microinjection buffer (10 mM Tris-HCl, pH 7.4, 0.25 mM EDTA in water) at the final concentrations 0.12 µM Cas9, 0.6 µM of each of the two crRNA:tracRNA complexes in microinjection buffer. Foster mother (minimum age 8 weeks) were set up with vasectomized males in a two to one ratio. Next day, pseudopregnant female (recognized by a copulation prop) were collected. For transplanting the injected oocytes, pseudopregnant female was anesthetized by an IP injection of a mix of Ketalin (12 mg/ml ketamine in PBS)-Rompun (0.61 xylazine mg/ml PBS) 100 µl per 10 g bodyweight). Post-surgery pain relief was given when the mouse was anaesthetized (S.C. Rimadyl Cattle, 5 mg/ml in PBS, dose 5 µg/g mouse). Transplantation resulted in 10 pups from two litters, of which two (one male one female) contained the deletions in the targeted region, as determined by PCR genotyping followed by cloning and sequencing of the PCR product. Another female contained an inversion of the region flanked by the CRISPR/Cas9 cuts; this was not used to establish a colony. Multiple primer combinations were tested during initial genotyping, but mB2i11-F1 AGCTGCCACATGGATTCTGAG, mB2i14-R1 ACATGCAGAGAACAGGGAGC, and mB2e12-R1 GCTTTTTGAAGGTGTTAAGGATTTT, were used routinely. The experimental cohort was eventually formed through back-crossing and inter-crossing from two founders, with the deletion produced by near-direct ligation between the two Cas9 cuts. Routine PCR genotyping of was performed using MyTaq Red mix (Bioline) and using the mentioned primers in 2:1:1 combination, for simultaneous amplification of the wild type and the Δ12 alleles (PCR products 663 and 770 bp, respectively).

Testes and ovaries were isolated from mice aged 6 to 32 weeks. Ovaries were also isolated from E15.5 embryos for collection of early meiotic prophase nuclei (leptotene, early zygotene for wild type and leptotene for mutant), and from E17.5 embryos for collection of late meiotic prophase nuclei (late zygotene and pachytene for wild type and early zygotene and late zygotene for mutant).

Periodic Acid Schiff (PAS) staining of mouse testes

Sections of paraffin-embedded gonads were mounted on slides. Paraffin was melted at 60°C for 60 min, and removed through three 5-minute washes of the slides in xylene. Subsequently, the slides were washed three times in 100% ethanol for 5 minutes. Next, the slides were incubated in 0.5% periodic acid

solution (Sigma-Aldrich 395132) for 5 minutes, and rinsed in distilled water. The slides were then incubated in Schiff reagent (Sigma-Aldrich, 3952016) for 15 minutes to stain the tissue, followed by washing the slides in lukewarm, streaming tap water for 5 min. Subsequently, the slides were counterstained with Hematoxylin solution (Klinipath 4085.9005) for 4 minutes and washed in streaming tap water for 5 minutes. The slides were embedded in Glycergel Mounting Medium (Dakocytomation, C0563) (heated to 45°C) and covered with a coverslip.

Hematoxylin-Eosin staining of mouse ovaries

Sections of in paraffin-embedded gonads were mounted on slides. Paraffin removal was performed as described above, and after two washes in 95% ethanol and one wash in 70% ethanol, the slides were stained with hematoxylin solution (Klinipath, 4085.9005) for 3 minutes and washed in streaming tap water for 5 minutes. Subsequently, the slides were stained for eosin Y (Sigma-Aldrich, HT110232) for 3 minutes, rinsed in tap water for 30 seconds, and dehydrated through 5 minutes 95% ethanol, two washes for 5 minutes 100% ethanol and two washes for 5 minutes xylene. The slides were embedded in DPX Mounting Medium (Merck, HX74511279) and covered with a coverslip.

Cell culture and clonogenic survival assay

Brca2$^{\Delta 12\text{-}14}$ and *Brca2*$^{\Delta 12}$ mES cells were engineered as described before [22], but using *Brca2*$^{GFP/GFP}$ cell line characterized in our previous publications [75,76] as the starting point instead of the *Hsf2bp*$^{GFP/GFP}$ cell line. mES cells were grown on gelatinized dishes in (0.1% gelatin in water) as described before [77] at atmospheric oxygen concentration in media comprising 1:1 mixture of DMEM (Lonza BioWhittaker Cat. BE12-604F/U1, with Ultraglutamine 1, 4.5 g/l Glucose) and BRL-conditioned DMEM, supplemented with 1000 U/ml leukemia inhibitory factor, 10% FCS, 1x NEAA, 200 U/ml penicillin, 200 µg/ml streptomycin, 89 µM β-mercaptoethanol. Clonogenic survival assays were performed in 6-well plates in technical duplicates. Two independent clones that genotyped homozygous for the deletion allele were used in each experiment and considered biological replicates. The experiment was performed three times (n=3 for the wild-type and n=6 for the mutant genotype). Untreated control wells were seeded with 200 cells per well in 2 mL media. Higher seeding densities of 800 and 2000 cells per well were used in the wells treated with higher drug concentrations. One day after seeding, the drugs were added: mitomycin C (MMC, Sigma, M4287-2MG), cisplatin, olaparib, talazoparib (BMN-673, Axon medchem, #2502). After 2-hour (MMC) or overnight (cisplatin, talazoparib) incubation, drug-containing media was removed, wells were rinsed with PBS and refilled with 2 mL fresh media. Colonies were stained (0.25% Coomassie briliant blue, 40% methanol, 10% acetic acid) on day 7 after seeding. Plates were photographed using a digital camera, images were analyzed using OpenCFU software [78] to quantify the colonies.

Meiotic spread nuclei preparation and immunocytochemistry

Nuclei of spermatocytes and oocytes were collected from gonads and spread as described previously [79,80] and stored at -80 °C. For immunocytochemistry, the protocol was described before [22]. In short, slides were washed with PBS, blocked, and incubated with primary antibody overnight. Subsequently, after washing with PBS, the slide was again blocked and incubated with secondary antibody for 2 hours. Finally, the slides were washed with PBS and embedded in Prolong Gold with DAPI (Invitrogen, p36931). The following primary antibodies were used: mouse anti-SYCP3 (1:200, Abcam ab97672), guinea pig anti-

SYCP3 [81](1:200), guinea pig anti-SYCP2 [82](1:100), mouse anti-DMC1 (1:1000, Abcam ab11054), rabbit anti-RAD51 [83](1:1000), rabbit anti-BRME1 [25] (1:100, #2), rabbit anti-HSF2BP [25] (1:30, #1), rabbit anti-RPA [84] (1:50), guinea pig anti-HORMAD2 [85] (1:100), rabbit anti-SPATA22 (1:100, Proteintech, 16989-1-AP). The following secondary antibodies were used: goat anti-rabbit Alexa 488 (1:500, Invitrogen A-11008), goat anti-mouse Alexa 555 (1:500, Invitrogen A-21422), goat anti-mouse Alexa 633 (1:500, Invitrogen A-21050), goat anti-guinea pig Alexa 546 (1:500, Invitrogen A-11074).

Microscopy and meiotic analysis

Immunostained nuclear spreads were imaged using a Zeiss Confocal Laser Scanning Microscope 700 with a 63x objective immersed in oil. Images within one analysis were analyzed with the same gain. Images were analyzed using Image J software[86] and to analyze the meiotic proteins we used methods as described before [22]. In short, for all proteins (RAD51, DMC1, BRME1, RPA, SPATA22 and HSF2BP) foci quantification was performed using Image J function “Analyze particles” in combination with a manual threshold. A mask of a synaptonemal complex marker (SYCP3, SYCP2, HORMAD2) was used to reduce detection of background signal. Particles smaller than 0.0196 μm^2 and larger than 0.98 μm^2 were excluded, except for HSF2BP where only particles smaller than 0.0294 m^2 were excluded. For HSF2BP, we also adjusted the particle count because of the variable HSF2BP intensity influencing the particle count, by taking into account the average size of 0.25 μm^2 of an HSF2BP particle (for details see ref. [22]).

Foci intensity for SPATA22, BRME1, RPA, and RAD51 (female only) was determined as follows: per focus, the intensity was measured and all foci values from a single nucleus were then averaged. For HSF2BP, the mean intensity within the SYCP3 mask was measured. All intensities were normalized by the mean intensity of SYCP3.

For RAD51 and DMC1 quantifications in spermatocytes, we re-used images from our previous publication [22] for two wild types (wt_mouse2 and wt_mouse3), and we also generated new images. For BRME1 quantifications in spermatocytes, we re-used images from the previous publication [22] for one wild type (wt_mouse3), and we also generated new images.

Meiotic sub-stages were classified into leptotene, early zygotene, late zygotene and pachytene, corresponding to observation of short chromosomal axes, longer chromosomal axes with some synapsis, long chromosomal axes with much synapsis and complete synapsed chromosomal axes, respectively.

For each meiotic protein staining, images from 2 or 3 different animals of each genotype were pooled as indicated in the figure legends. The number of analyzed nuclei is indicated in the figures.

Fluorescent in situ hybridization (FISH)

FISH was combined with immunostaining on meiotic spread spermatocytes. First, the immunostaining of SYCP3 (mouse anti-SYCP3, 1:200, Abcam ab97672, combined with Alexa 555) was performed as described above. Thereafter, the slides were washed 10 min in 2x SSC (pH 7.5) at 55°C, followed by 5 min washing in 2x SSC at room temperature. The slides were dehydrated using an ethanol series: 1x 5 min 70% ethanol, 1x 5 min 90% ethanol, 2x 5 min 100% ethanol and finally the slides were dried for 5 min at room temperature. Next, 15 µl of the probe painting mouse chromosome 13 (X Cyting Mouse Chromosome Painting Probe for chromosome 13 in green, D-1413-050-FI) was applied on the slide and covered with a coverslip and sealed with photo glue. The sample and probe were denatured for 2.5 min at 78°C on a heating plate. The plate was turned off and the slides were left on the plate for 30 min, followed by

incubation at 37°C in a humid box overnight. The next day the protocol of the probe supplier for washing and mounting was followed. In short, the photo glue and coverslip were removed, subsequently the slides were incubated with 0.4x SSC (pH 7) at 72 °C for 2 min and then washed with 2x SSC with 0.05% Tween-20 (pH 7) for 30 seconds. Subsequently, the slides were rinsed with distilled water and air dried. Finally, the slides were mounted with Prolong Gold Antifade Mountant with DAPI.

In total, 152 images of *Brca2*$^{\Delta 12\text{-}14}$ spermatocytes (from two different animals) were acquired using a confocal microscope (as described above) and manually scored for number of FISH clouds and degree of synapsis. Nuclei for which the number of FISH clouds was unclear, were excluded from further analysis (30 images in total).

The number of fully synapsed chromosomes was quantified manually. STED images of nuclear spreads of *Spo11*$^{-/-}$ spermatocytes immunostained for SYCP3 originated from the data we collected for our recent publication [72]. For *Brca2*$^{\Delta 12\text{-}14}$, the SIM images of nuclear spreads of *Brca2*$^{\Delta 12\text{-}14}$ spermatocytes were analyzed (see below). In total, 24 *Spo11*$^{-/-}$ nuclei and 16 *Brca2*$^{\Delta 12\text{-}14}$ nuclei were used for this analysis, both collected from two different animals.

Expression and purification of DMC1

Construct pAZ379 for bacterial expression of human his-TEV-DMC1 was engineered by subcloning DMC1 coding sequence into pETM-11 vector using Gibson assembly. Rosetta2 DE3 pLysS *E. coli* strain was transformed with the construct and plated on selective (50 µg/mL kanamycin, 30 µg/mL chloramphenicol) LB-agar plates. Ten colonies were used to inoculate 200 mL selective LB media, the culture was grown overnight at 37 °C with shaking, and used to inoculate 9 L selective LB media. The 9 L culture was grown at 37 °C till OD_{600} reached 0.6-0.8, expression was induced by adding IPTG to 0.2 mM final concentration. Cells were cultured for another 3 h at 37 °C, collected by centrifugation and frozen. The pellet was thawed in two volumes of lysis buffer (3M NaCl, 100mM Tris pH7,5, 10% Glycerol, 0.5mM EDTA, 5 mM β-mercaptoethanol, protease inhibitors (Roche)) and sonicated on ice (10 pulses of 10 seconds). The lysate was incubated overnight at 4 °C on a rotator, and then cleared by centrifugation at 22000× rcf for 45 minutes at 4 °C. Cleared supernatant was supplemented with 5 mM imidazole and incubated with washed (500mM NaCl, 25mM Tris pH8, 10% Glycerol, 0.5mM EDTA, 1mM DTT) Ni-NTA beads for 1h at 4 °C on a rotator. Beads were washed with 20 mM and 40 mM imidazole (two times 10 mL for each wash). Bound protein was eluted with 400 mM imidazole, fractions analyzed by electrophoresis and pooled, supplemented with TEV protease and dialyzed overnight against 2 L of 150mM NaCl, 10% Glycerol, 50mM Tris pH 8, 5mM β-mercaptoethanol. Protein was further purified using 5 mL HiTrap heparine with a 15CV gradient elution from 150 to 1000 mM NaCl in 25mM Tris pH 8, 10% Glycerol, 1mM DTT. Fractions were pooled and diluted to 100mM NaCl and loaded on a 1ml CaptoQ column. Protein was eluted with a 10CV gradient from 100-1000mM NaCl in 25mM Tris pH 8, 10% Glycerol, 1mM DTT. Fractions were pooled and aliquots were frozen in liquid nitrogen and stored at -80°C.

Expression and purification of RAD51

The human RAD51 was purified from *E. coli* as previously described [87–89]. Briefly: The cell pellet containing expressed untagged RAD15 was thawed in two volumes of lysis buffer (3M NaCl, 100mM Tris pH7,5, 10% Glycerol, 4mM EDTA, 20 mM β-mercaptoethanol, protease inhibitors (Roche)) and sonicated on ice (10 pulses of 10 seconds). The lysate was incubated overnight at 4 °C. To cleared supernatant ½ volume of

4M ammonium sulphate was slowly added while stirring on ice for 1hr. After spinning down, the pellet was dissolved in buffer and dialysed overnight. Spin down again and dissolve pellet in buffer (600mM NaCl, 25mM Tris pH7,5, 5% Glycerol, 1mM DTT) for 2hr. Dilute slowly to 200mM and load on 5ml Hitrap Heparine column. Elute with gradient to 1M NaCl. Further purify with Superdex 200 16/60 and final 1ml Hitrap Heparine column.

Expression and purification of GST-BRCA2 F2s3

Constructs pAZ388 (wt) and pAZ404 (F2406A) for bacterial expression of human his-GST-TEV-BRCA2 F2S3 (aa2379-2433) were engineered by subcloning BRCA2 coding sequence into pETM-30 vector using Gibson assembly. Rosetta2 DE3 pLysS *E. coli* strain was transformed with the construct and plated on selective (50 µg/mL kanamycin, 30 µg/mL chloramphenicol) LB-agar plates. An overnight culture of a few colonies was grown at 37 °C. 3 liter culture was inoculated with overnight culture and grown at 37 °C till OD600 reached 0.5-0.7, expression was induced by adding IPTG to 0.2 mM final concentration. Cells were cultured for another 3 h at 37 °C, collected by centrifugation and frozen. The pellet was thawed in an equal volume of lysis buffer (1M NaCl, 25mM Tris pH7,5, 5% Glycerol,1mM DTT, protease inhibitors (Roche)) and sonicated on ice (10 pulses of 10 seconds). The lysate was cleared by centrifugation at 22000rcf for 45 minutes at 4 °C. Cleared supernatant was supplemented with 10 mM imidazole and loaded on a 5ml Histrap HP (Cytiva) column, prewashed with buffer buffer A (500mM NaCl, 25mM Tris pH7,5, 5% Glycerol, 10mM Imidazol, 1mM DTT). Wash 3CV with buffer A and elute with 5CV buffer B (500mM NaCl, 25mM Tris pH7,5, 5% Glycerol, 250mM Imidazol, 1mM DTT). Fractions were collected an dilute to final 100mM NaCl, 25mM Tris pH8,8, 5% Glycerol, 1mM DTT and load on 5ml Hitrap Q (Cytiva). Wash 3CV and elute with 5CV gradient to 1M NaCl, 25mM Tris pH8,8, 5% Glycerol, 1mM DTT. Peak fractions were collected and loaded on Superdex 75 16/60 column. Fractions were pooled and aliquots were frozen in liquid nitrogen and stored at -80°C.

GST pull-down assay with immunoblot detection

Bacterial expression constructs for expression of his-GST-TEV-tagged BRCA2 fragments and their amino acid substitution variants were engineered using Gibson assembly in pETM-30 vector and sequence-verified. Constructs were transformed into Rosetta2 DE3 pLysS *E. coli* expression strain. Two mL of selective LB (50 µg/mL kanamycin, 30 µg/mL chloramphenicol) media was inoculated, the culture was grown overnight at 37 °C with shaking, diluted to 10 mL, further incubated till OD_{600} reached 0.6-0.8, induced with 0.2 mM IPTG, grown for additional 3 h at 37°. Cells were collected by centrifugation, pellet was resuspended in 1 mL NETT+DP buffer (NaCl 100 mM, Tris-HCl pH 7.5 50 mM, EDTA pH 8 5 mM, Triton X100 0.5%, freshly supplemented with protease inhibitors (Roche), 1 mM DTT, 1 mM PMSF) and sonicated (10× 5 sec on, 10 sec off). Lysate was transferred to Eppendorf minicentrifuge tubes and cleared by centrifugation in (30 min at 4 °C). Supernatant was mixed with 20 µL GSH-Sepharose beads (GE Healthcare 17-5132-01) and incubated overnight at 4 °C. Beads were collected by centrifugation (500 rcf, 2 min, 4 °C), washed with NETT+ buffer ((NaCl 100 mM, Tris-HCl pH 7.5 50 mM, EDTA pH 8 5 mM, Triton X100 0.5%, freshly supplemented with protease inhibitors (Roche)), and incubated with DMC1 protein solution (~2 µg in 1 mL NETT+) for 1.5 h at 4 °C. Prior to incubation, bead suspension was vortexed, a 40 µL aliquot was collected as input, mixed with 12 µL 5× sample buffer (50% glycerol, 250 mM Tris HCl pH 6.8, 10% SDS, 0.5% bromophenol blue, 0.5 M β-mercaptoethanol) and denature for 5 min at 95 °C. After

incubation with DMC1, beads were washed three times with NETT+ buffer and incubated with 25 µL of Laemmli sample buffer for 5 min at 95 °C to elute bound proteins. Samples (5 µL of eluate) were run on a 13% tris-glycine acrylamide gel, transferred to PVDF membrane, blocked (5% skim milk in PBS-T (PBS with 0.05% Tween-20)) and immunodetected with a mixture of rabbit anti-RAD51 pAb (1:20000 [83]) and mouse anti-GST mAb (1:5000, B-14 Santa Cruz, sc-138) antibodies overnight. After washes, the membranes were incubated with fluorescently-labelled secondary antibodies (anti-mouse CF680 (Sigma #SAB460199), anti-rabbit CF770 (Sigma #SAB460215)), washed (5 × 5 min PBS-T) and scanned using Odyssey CLx imaging system (LI-COR).

GST-pull down with protein staining

10µl magnetic glutathione beads (Pierce #88821) were prewashed with buffer (200mM NaCl, 25mM Tris pH7,5, 5% Glycerol, 1mM DTT). 120µg (saturating) of GST or GST-BRCA2 F2S3 was incubated with the beads for 1hr at 4°C. Beads were washed 3x with buffer. 70µg of DMC1 or RAD51 was added and incubated for 1hr at 4°C. Beads were washed 3x with buffer. To the beads 40µl buffer and 10µl 5x sample loading buffer was added. Samples were boiled 5min at 90°C and 10µl was loaded on a 4-20% gradient SDS-PAGE gel (Biorad #4561096). Gel was stained with Coomassie brilliant blue R.

Isothermal titration calorimetry

Interactions between the DMC1 protein and the synthetic BRCA2 peptides were characterized using a VP-ITC Calorimeter (GE Healthcare). The peptides tested were wild type and F2406A variant of the PhePP (F2s6) fragment and the peptide from the C-terminal RAD51-binding TR2 region (3288-3303) The experiments were performed at 20 °C and duplicated; interactions with F2406A and TR2 were also tested at 10 °C. The buffer was 25 mM Tris buffer, pH 7.5, 100 mM NaCl and 5 mM β-mercaptoethanol. 10 µM of DMC1 in the cell was titrated with 100 µM of BRCA2 peptide in the injection syringe; 10 µL of the syringe volume were injected every 210 s. Data recording were performed using the Origin 7.0 software provided by the manufacturer.

Structured illumination microscopy (SIM) imaging and analysis

SIM images were acquired on a Zeiss Elyra PS1 system using a 63x 1.40 NA oil immersion objective equipped with an 512x512 Andor Ixon Du 897 EMCCD camera, using five phases and five rotations of the illumination. Diode lasers with a wavelength of 488 and 561 nm were used in combination with an emission filter (BP 495-575 + LP 750, BP 570-650 + LP 750). For a SIM image, a z-stack of 21 images was taken with an optimal interval. Images were taken with a laser power between 2 and 5, exposure time of 100 ms and an EMCCD gain based on strong signal intensity, but without saturation. Reconstruction of the SIM data was performed using ZEN2012 software (Carl Zeiss). To generate a single plane image, the most in focus image was selected from the z-stack.

Coordinate determination of RPA foci and synaptonemal complex in SIM images was performed as follows: the coordinates of the synaptonemal complex were determined by selecting a mask of the axes with a Gaussian Blur (sigma of 2), followed by an automatic threshold (Default dark) which was manually checked and using the Image J function “Analyze Particles” only particles larger than 0.2 μm^2 were included. The mask was dilated by 238.2 nm and of this mask a selection was created to remove all RPA

signal outside of the mask. Using the Image J functions “Skeletonize” and “Points from Mask” the coordinates along the center of the SYCP3 mask were determined. The RPA foci were detected using the Image J function “Find Maxima” with a manually set prominence. Using both coordinates, the shortest distance of RPA foci to the skeletonized center of SYCP3 was calculated. In the violin plot distances larger than 500 nm were plotted as 500 nm. For the nearest neighbor analysis all RPA foci within a nucleus were used and for each RPA focus the nearest RPA focus was determined. The distance between this nearest neighbor pair was plotted in a density plot. Distances larger than 1500 nm were plotted as 1500 nm. For the distance and nearest neighbor analysis, 13 nuclei of wild type zygotene spermatocytes and 16 nuclei of *Brca2*$^{\Delta 12\text{-}14}$ zygotene spermatocytes (originating from 2 different animals per genotype) were used and 9 nuclei of wild type zygotene oocytes and 14 nuclei of *Brca2*$^{\Delta 12\text{-}14}$ zygotene oocytes (originating from 2 different animals per genotype) were used.

RPA tether identification

RPA tethers are characterized as an RPA focus (or foci) often localized between positions along chromosomal axes, indicating that the RPA focus is present on an invisible line which connects the chromosomal axes. The context of the RPA tether was scored manually, and was divided into three groups: RPA tether in a context of an early structure (no alignment and no synapsis), RPA tether in the context of a mid-structure (alignment (parallel orientation of chromosomal axes at the distance larger than synapsis) and no synapsis) and RPA tether in the context of a late structure (synapsis). OF each RPA tether we also indicated the presence of kinks in the chromosomal axes. The presence of kinks was determined based on the degree of deflection of the chromosomal axes around the RPA tether. We analyzed 27 wild type and 16 *Brca2*$^{\Delta 12\text{-}14}$ spermatocytes, both from two different animals. The butterfly configuration was characterized based on a RPA tether, kinks in both, complete, chromosomal axes.

Statistical analysis

For the meiotic data the statistical analysis was performed using GraphPad Prism software (version 9) and R (version 4.0.3). For the confocal foci count the statistical significance was determined using unpaired student t-test comparing wild type with *Brca2*$^{\Delta 12\text{-}14}$ in different meiotic stages. For the SIM data, statistical significance was determined using a Wilcoxon test, unpaired student t-test or Kolmogorov–Smirnov test, as indicated in the text or figure legend. The number of analyzed nuclei (collected from 2 or 3 different animals per genotype) is in indicated in the graph, text and/or figure legend.

REFERENCES

1. Holloman, W.K. (2011). Unraveling the mechanism of BRCA2 in homologous recombination. Nat Struct Mol Biol *18*, 748–754. 10.1038/nsmb.2096.

2. Zelensky, A.N., Kanaar, R., and Wyman, C. (2014). Mediators of Homologous DNA Pairing. Csh Perspect Biol *6*, a016451–a016451. 10.1101/cshperspect.a016451.

3. Kojic, M., Kostrub, C.F., Buchman, A.R., and Holloman, W.K. (2002). BRCA2 Homolog Required for Proficiency in DNA Repair, Recombination, and Genome Stability in Ustilago maydis. Mol Cell *10*, 683–691. 10.1016/s1097-2765(02)00632-9.

4. Siaud, N., Dray, E., Gy, I., Gérard, E., Takvorian, N., and Doutriaux, M.-P. (2004). Brca2 is involved in meiosis in Arabidopsis thaliana as suggested by its interaction with Dmc1. Embo J *23*, 1392–1401. 10.1038/sj.emboj.7600146.

5. Fu, R., Wang, C., Shen, H., Zhang, J., Higgins, J.D., and Liang, W. (2020). Rice OsBRCA2 Is Required for DNA Double-Strand Break Repair in Meiotic Cells. Front Plant Sci *11*, 600820. 10.3389/fpls.2020.600820.

6. Yoshikawa, Y., Kimura, S., Soga, A., Sugiyama, M., Ueno, A., Kondo, H., Zhu, Z., Ochiai, K., Nakayama, K., Hakozaki, J., et al. (2022). Plasmodium berghei Brca2 is required for normal development and differentiation in mice and mosquitoes. Parasite Vector *15*, 244. 10.1186/s13071-022-05357-w.

7. Weinberg-Shukron, A., Rachmiel, M., Renbaum, P., Gulsuner, S., Walsh, T., Lobel, O., Dreifuss, A., Ben-Moshe, A., Zeligson, S., Segel, R., et al. (2018). Essential Role of BRCA2 in Ovarian Development and Function. The New England journal of medicine *379*, 1042–1049. 10.1056/nejmoa1800024.

8. Klovstad, M., Abdu, U., and Schüpbach, T. (2008). Drosophila brca2 Is Required for Mitotic and Meiotic DNA Repair and Efficient Activation of the Meiotic Recombination Checkpoint. Plos Genet *4*, e31. 10.1371/journal.pgen.0040031.

9. Ko, E., Lee, J., and Lee, H. (2008). Essential role of brc-2 in chromosome integrity of germ cells in C. elegans. Mol Cells *26*, 590–594.

10. Martin, J.S., Winkelmann, N., Petalcorin, M.I.R., Mcilwraith, M.J., and Boulton, S.J. (2005). RAD-51-dependent and -independent roles of a Caenorhabditis elegans BRCA2-related protein during DNA double-strand break repair. Mol Cell Biol *25*, 3127–3139. 10.1128/mcb.25.8.3127-3139.2005.

11. Sharan, S.K., Pyle, A., Coppola, V., Babus, J., Swaminathan, S., Benedict, J., Swing, D., Martin, B.K., Tessarollo, L., Evans, J.P., et al. (2004). BRCA2 deficiency in mice leads to meiotic impairment and infertility. Development (Cambridge, England) *131*, 131–142. 10.1242/dev.00888.

12. Friedman, L.S., Thistlethwaite, F.C., Patel, K.J., Yu, V.P., Lee, H., Venkitaraman, A.R., Abel, K.J., Carlton, M.B., Hunter, S.M., Colledge, W.H., et al. (1998). Thymic lymphomas in mice with a truncating mutation in Brca2. Cancer Res *58*, 1338–1343.

13. Connor, F., Bertwistle, D., Mee, P.J., Ross, G.M., Swift, S., Grigorieva, E., Tybulewicz, V.L., and Ashworth, A. (1997). Tumorigenesis and a DNA repair defect in mice with a truncating Brca2 mutation. Nat Genet *17*, 423 430. 10.1038/ng1297-423.

14. Martinez, J.S., Nicolai, C. von, Kim, T., Ehlen, A., Mazin, A.V., Kowalczykowski, S.C., and Carreira, A. (2016). BRCA2 regulates DMC1-mediated recombination through the BRC repeats. Proc National Acad Sci *113*, 3515–3520. 10.1073/pnas.1601691113.

15. Seeliger, K., Dukowic-Schulze, S., Wurz-Wildersinn, R., Pacher, M., and Puchta, H. (2012). BRCA2 is a mediator of RAD51- and DMC1-facilitated homologous recombination in Arabidopsis thaliana. New Phytol *193*, 364–375. 10.1111/j.1469-8137.2011.03947.x.

16. Thorslund, T., Esashi, F., and West, S.C. (2007). Interactions between human BRCA2 protein and the meiosis-specific recombinase DMC1. Embo J *26*, 2915–2922. 10.1038/sj.emboj.7601739.

17. Dray, E., Siaud, N., Dubois, E., and Doutriaux, M.-P. (2006). Interaction between Arabidopsis Brca2 and its partners Rad51, Dmc1, and Dss1. Plant Physiol *140*, 1059–1069. 10.1104/pp.105.075838.

18. Biswas, K., Das, R., Eggington, J.M., Qiao, H., North, S.L., Stauffer, S., Burkett, S.S., Martin, B.K., Southon, E., Sizemore, S.C., et al. (2012). Functional evaluation of BRCA2 variants mapping to the PALB2-binding and C-terminal DNA-binding domains using a mouse ES cell-based assay. Hum Mol Genet *21*, 3993 4006. 10.1093/hmg/dds222.

19. Zhang, J., Fujiwara, Y., Yamamoto, S., and Shibuya, H. (2019). A meiosis-specific BRCA2 binding protein recruits recombinases to DNA double-strand breaks to ensure homologous recombination. Nat Commun *10*, 722. 10.1038/s41467-019-08676-2.

20. Brandsma, I., Odijk, H., Oostra, A., Dekkers, D., Bezstarosti, K., Tempel, N. van den, Demmers, J., Dorsman, J., Gent, D. van, Kanaar, R., et al. (2016). Overexpression of HSF2BP, a new BRCA2 interactor, results in a Fanconi anemia-like phenotype. In Balancing Pathways in DNA Double Strand Break Repair, pp. 98–140.

21. Brandsma, I., Sato, K., Rossum-Fikkert, S.E. van, Vliet, N. van, Sleddens, E., Reuter, M., Odijk, H., Tempel, N. van den, Dekkers, D.H.W., Bezstarosti, K., et al. (2019). HSF2BP Interacts with a Conserved Domain of BRCA2 and Is Required for Mouse Spermatogenesis. Cell Reports *27*, 3790-3798.e7. 10.1016/j.celrep.2019.05.096.

22. Ghouil, R., Miron, S., Koornneef, L., Veerman, J., Paul, M.W., Du, M.-H.L., Sleddens-Linkels, E., Rossum-Fikkert, S.E. van, Loon, Y. van, Felipe-Medina, N., et al. (2021). BRCA2 binding through a cryptic repeated motif to HSF2BP oligomers does not impact meiotic recombination. Nat Commun *12*, 4605. 10.1038/s41467-021-24871-6.

23. Sato, K., Brandsma, I., van Rossum-Fikkert, S.E., Verkaik, N., Oostra, A.B., Dorsman, J.C., van Gent, D.C., Knipscheer, P., Kanaar, R., and Zelensky, A.N. (2020). HSF2BP negatively regulates homologous recombination in DNA interstrand crosslink repair. Nucleic Acids Res *48*, 2442–2456. 10.1093/nar/gkz1219.

24. Pendlebury, D.F., Zhang, J., Agrawal, R., Shibuya, H., and Nandakumar, J. (2021). Structure of a meiosis-specific complex central to BRCA2 localization at recombination sites. Nat Struct Mol Biol *28*, 671–680. 10.1038/s41594-021-00635-0.

25. Felipe-Medina, N., Caburet, S., Sánchez-Sáez, F., Condezo, Y.B., Rooij, D.G. de, Gómez-H, L., Garcia-Valiente, R., Todeschini, A.L., Duque, P., Sánchez-Martin, M.A., et al. (2020). A missense in HSF2BP causing Primary Ovarian Insufficiency affects meiotic recombination by its novel interactor C19ORF57/BRME1. Elife *9*, e56996. 10.7554/elife.56996.

26. Shang, Y., Huang, T., Liu, H., Liu, Y., Liang, H., Yu, X., Li, M., Zhai, B., Yang, X., Wei, Y., et al. (2020). MEIOK21: a new component of meiotic recombination bridges required for spermatogenesis. Nucleic Acids Res *48*, gkaa406. 10.1093/nar/gkaa406.

27. Takemoto, K., Tani, N., Takada-Horisawa, Y., Fujimura, S., Tanno, N., Yamane, M., Okamura, K., Sugimoto, M., Araki, K., and Ishiguro, K.-I. (2020). Meiosis-Specific C19orf57/4930432K21Rik/BRME1 Modulates Localization of RAD51 and DMC1 to DSBs in Mouse Meiotic Recombination. Cell Reports *31*, 107686. 10.1016/j.celrep.2020.107686.

28. Zhang, J., Gurusaran, M., Fujiwara, Y., Zhang, K., Echbarthi, M., Vorontsov, E., Guo, R., Pendlebury, D.F., Alam, I., Livera, G., et al. (2020). The BRCA2-MEILB2-BRME1 complex governs meiotic recombination and impairs the mitotic BRCA2-RAD51 function in cancer cells. Nat Commun *11*, 2055. 10.1038/s41467-020-15954-x.

29. Li, M., Feng, H., Lin, Z., Zheng, J., Liu, D., Guo, R., Li, J., Li, R.H.W., Ng, E.H.Y., Huen, M.S.Y., et al. (2020). The novel male meiosis recombination regulator coordinates the progression of meiosis prophase I. J Genet Genomics *47*, 451–465. 10.1016/j.jgg.2020.08.001.

30. Baudat, F., Manova, K., Yuen, J.P., Jasin, M., and Keeney, S. (2000). Chromosome Synapsis Defects and Sexually Dimorphic Meiotic Progression in Mice Lacking Spo11. Mol Cell *6*, 989–998. 10.1016/s1097-2765(00)00098-8.

31. Carofiglio, F., Sleddens-Linkels, E., Wassenaar, E., Inagaki, A., Cappellen, W.A. van, Grootegoed, J.A., Toth, A., and Baarends, W.M. (2018). Repair of exogenous DNA double-strand breaks promotes chromosome synapsis in SPO11-mutant mouse meiocytes, and is altered in the absence of HORMAD1. Dna Repair *63*, 25 38. 10.1016/j.dnarep.2018.01.007.

32. Pittman, D.L., Cobb, J., Schimenti, K.J., Wilson, L.A., Cooper, D.M., Brignull, E., Handel, M.A., and Schimenti, J.C. (1998). Meiotic Prophase Arrest with Failure of Chromosome Synapsis in Mice Deficient for Dmc1, a Germline-Specific RecA Homolog. Mol Cell *1*, 697–705. 10.1016/s1097-2765(00)80069-6.

33. Yoshida, K., Kondoh, G., Matsuda, Y., Habu, T., Nishimune, Y., and Morita, T. (1998). The Mouse RecA-like Gene Dmc1 Is Required for Homologous Chromosome Synapsis during Meiosis. Mol Cell *1*, 707–718. 10.1016/s1097-2765(00)80070-2.

34. Salle, S.L., Palmer, K., O'Brien, M., Schimenti, J.C., Eppig, J., and Handel, M.A. (2012). Spata22, a Novel Vertebrate-Specific Gene, Is Required for Meiotic Progress in Mouse Germ Cells. Biol Reprod *86*, Article 45, 1-12. 10.1095/biolreprod.111.095752.

35. Ribeiro, J., Dupaigne, P., Petrillo, C., Ducrot, C., Duquenne, C., Veaute, X., Saintomé, C., Busso, D., Guerois, R., Martini, E., et al. (2021). The meiosis-specific MEIOB–SPATA22 complex cooperates with RPA to form a compacted mixed MEIOB/SPATA22/RPA/ssDNA complex. Dna Repair *102*, 103097. 10.1016/j.dnarep.2021.103097.

36. Ishishita, S., Matsuda, Y., and Kitada, K. (2014). Genetic evidence suggests that Spata22 is required for the maintenance of Rad51 foci in mammalian meiosis. Sci Rep-uk *4*, 6148. 10.1038/srep06148.

37. Shang, Y., Huang, J., Li, W., Zhang, Y., Zhou, X., Shao, Q., Tan, T., Yin, S., Zhang, L., and Wang, S. (2022). MEIOK21 regulates oocyte quantity and quality via modulating meiotic recombination. Faseb J *36*, e22357. 10.1096/fj.202101950r.

38. Kwon, Y., Rösner, H., Zhao, W., Selemenakis, P., He, Z., Kawale, A.S., Katz, J.N., Rogers, C.M., Neal, F.E., Shabestari, A.B., et al. (2023). DNA binding and RAD51 engagement by the BRCA2 C-terminus orchestrate DNA repair and replication fork preservation. Nat Commun *14*, 432. 10.1038/s41467-023-36211-x.

39. Oliver-Bonet, M., Campillo, M., Turek, P.J., Ko, E., and Martin, R.H. (2007). Analysis of replication protein A (RPA) in human spermatogenesis. Mhr Basic Sci Reproductive Medicine *13*, 837–844. 10.1093/molehr/gam076.

40. Moens, P.B., Kolas, N.K., Tarsounas, M., Marcon, E., Cohen, P.E., and Spyropoulos, B. (2002). The time course and chromosomal localization of recombination-related proteins at meiosis in the mouse are compatible with models that can resolve the early DNA-DNA interactions without reciprocal recombination. J Cell Sci *115*, 1611–1622. 10.1242/jcs.115.8.1611.

41. Moens, P.B., Marcon, E., Shore, J.S., Kochakpour, N., and Spyropoulos, B. (2007). Initiation and resolution of interhomolog connections: crossover and non-crossover sites along mouse synaptonemal complexes. J Cell Sci *120*, 1017–1027. 10.1242/jcs.03394.

42. Blokhina, Y.P., Nguyen, A.D., Draper, B.W., and Burgess, S.M. (2019). The telomere bouquet is a hub where meiotic double-strand breaks, synapsis, and stable homolog juxtaposition are coordinated in the zebrafish, Danio rerio. Plos Genet *15*, e1007730. 10.1371/journal.pgen.1007730.

43. Luo, M., Yang, F., Leu, N.A., Landaiche, J., Handel, M.A., Benavente, R., Salle, S.L., and Wang, P.J. (2013). MEIOB exhibits single-stranded DNA-binding and exonuclease activities and is essential for meiotic recombination. Nat Commun *4*, 2788. 10.1038/ncomms3788.

44. Mesman, R.L.S., Calléja, F.M.G.R., Hoya, M. de la, Devilee, P., Asperen, C.J. van, Vrieling, H., and Vreeswijk, M.P.G. (2020). Alternative mRNA splicing can attenuate the pathogenicity of presumed loss-of-function variants in BRCA2. Genet Med *22*, 1355–1365. 10.1038/s41436-020-0814-5.

45. Guidugli, L., Shimelis, H., Masica, D.L., Pankratz, V.S., Lipton, G.B., Singh, N., Hu, C., Monteiro, A.N.A., Lindor, N.M., Goldgar, D.E., et al. (2018). Assessment of the Clinical Relevance of BRCA2 Missense Variants by Functional and Computational Approaches. Am J Hum Genetics *102*, 233–248. 10.1016/j.ajhg.2017.12.013.

46. Davies, O.R., and Pellegrini, L. (2007). Interaction with the BRCA2 C terminus protects RAD51-DNA filaments from disassembly by BRC repeats. Nat Struct Mol Biol *14*, 475 483. 10.1038/nsmb1251.

47. Miron, S., Legrand, P., Rossum-Fikkert, S.E. van, Ristic, D., Badar, A., Kanaar, R., Zinn-Justin, S., and Zelensky, A.N. (2023). DMC1 and RAD51 bind FxxA and FxPP motifs of BRCA2 via two separate interfaces. bioRxiv. 10.1101/2023.10.05.561053.

48. Moses, M.J., Poorman, P.A., Roderick, T.H., and Davisson, M.T. (1982). Synaptonemal complex analysis of mouse chromosomal rearrangements. Chromosoma *84*, 457–474. 10.1007/bf00292848.

49. Torgasheva, A.A., Rubtsov, N.B., and Borodin, P.M. (2013). Recombination and synaptic adjustment in oocytes of mice heterozygous for a large paracentric inversion. Chromosome Res *21*, 37–48. 10.1007/s10577-012-9336-6.

50. Yoon, S., Choi, E.-H., Kim, J.-W., and Kim, K.P. (2018). Structured illumination microscopy imaging reveals localization of replication protein A between chromosome lateral elements during mammalian meiosis. Exp Mol Medicine *50*, 112. 10.1038/s12276-018-0139-5.

51. Ishiguro, K.-I. (2022). Sexually Dimorphic Properties in Meiotic Chromosome. Sex Dev, 1–11. 10.1159/000520682.

52. Rotheneder, M., Stakyte, K., Logt, E. van de, Bartho, J.D., Lammens, K., Fan, Y., Alt, A., Kessler, B., Jung, C., Roos, W.P., et al. (2023). Cryo-EM structure of the Mre11-Rad50-Nbs1 complex reveals the molecular mechanism of scaffolding functions. Mol Cell *83*, 167-185.e9. 10.1016/j.molcel.2022.12.003.

53. Jager, M. de, Noort, J. van, Gent, D.C. van, Dekker, C., Kanaar, R., and Wyman, C. (2001). Human Rad50/Mre11 Is a Flexible Complex that Can Tether DNA Ends. Mol Cell *8*, 1129–1135. 10.1016/s1097-2765(01)00381-1.

54. Prieler, S., Chen, D., Huang, L., Mayrhofer, E., Zsótér, S., Vesely, M., Mbogning, J., and Klein, F. (2021). Spo11 generates gaps through concerted cuts at sites of topological stress. Nature *594*, 577–582. 10.1038/s41586-021-03632-x.

55. Johnson, D., Crawford, M., Cooper, T., Bouuaert, C.C., Keeney, S., Llorente, B., Garcia, V., and Neale, M.J. (2021). Concerted cutting by Spo11 illuminates meiotic DNA break mechanics. Nature *594*, 572–576. 10.1038/s41586-021-03389-3.

56. Albini, S.M., and Jones, G.H. (1987). Synaptonemal complex spreading in Allium cepa and A. fistulosum. Chromosoma *95*, 324–338. 10.1007/bf00293179.

57. Zickler, D., and Kleckner, N. (1999). Meiotic Chromosomes: Integrating Structure and Function. Annu Rev Genet *33*, 603–754. 10.1146/annurev.genet.33.1.603.

58. Dubois, E., Muyt, A.D., Soyer, J.L., Budin, K., Legras, M., Piolot, T., Debuchy, R., Kleckner, N., Zickler, D., and Espagne, E. (2019). Building bridges to move recombination complexes. P Natl Acad Sci Usa *116*, 12400–12409. 10.1073/pnas.1901237116.

59. Storlazzi, A., Gargano, S., Ruprich-Robert, G., Falque, M., David, M., Kleckner, N., and Zickler, D. (2010). Recombination Proteins Mediate Meiotic Spatial Chromosome Organization and Pairing. Cell *141*, 94–106. 10.1016/j.cell.2010.02.041.

60. King, G.A., Gross, P., Bockelmann, U., Modesti, M., Wuite, G.J.L., and Peterman, E.J.G. (2013). Revealing the competition between peeled ssDNA, melting bubbles, and S-DNA during DNA overstretching using fluorescence microscopy. Proc National Acad Sci *110*, 3859–3864. 10.1073/pnas.1213676110.

61. Mameren, J. van, Gross, P., Farge, G., Hooijman, P., Modesti, M., Falkenberg, M., Wuite, G.J.L., and Peterman, E.J.G. (2009). Unraveling the structure of DNA during overstretching by using multicolor, single-molecule fluorescence imaging. Proc National Acad Sci *106*, 18231–18236. 10.1073/pnas.0904322106.

62. Chan, K.L., and Hickson, I.D. (2011). New insights into the formation and resolution of ultra-fine anaphase bridges. Semin Cell Dev Biol *22*, 906–912. 10.1016/j.semcdb.2011.07.001.

63. Lui, D.Y., Peoples-Holst, T.L., Mell, J.C., Wu, H.-Y., Dean, E.W., and Burgess, S.M. (2006). Analysis of Close Stable Homolog Juxtaposition During Meiosis in Mutants of Saccharomyces cerevisiae. Genetics *173*, 1207–1222. 10.1534/genetics.105.050658.

64. Tessé, S., Storlazzi, A., Kleckner, N., Gargano, S., and Zickler, D. (2003). Localization and roles of Ski8p protein in Sordaria meiosis and delineation of three mechanistically distinct steps of meiotic homolog juxtaposition. Proc National Acad Sci *100*, 12865–12870. 10.1073/pnas.2034282100.

65. Storlazzi, A., Tessé, S., Gargano, S., James, F., Kleckner, N., and Zickler, D. (2003). Meiotic double-strand breaks at the interface of chromosome movement, chromosome remodeling, and reductional division. Gene Dev *17*, 2675–2687. 10.1101/gad.275203.

66. Zickler, D. (2006). From early homologue recognition to synaptonemal complex formation. Chromosoma *115*, 158–174. 10.1007/s00412-006-0048-6.

67. Zickler, D., and Kleckner, N. (2015). Recombination, Pairing, and Synapsis of Homologs during Meiosis. Csh Perspect Biol *7*. 10.1101/cshperspect.a016626.

68. Newman, T.A.C., Beltran, B., McGehee, J.M., Elnatan, D., Cahoon, C.K., Paddy, M.R., Chu, D.B., Spakowitz, A.J., and Burgess, S.M. (2022). Diffusion and distal linkages govern interchromosomal dynamics during meiotic prophase. Proc National Acad Sci *119*, e2115883119. 10.1073/pnas.2115883119.

69. Marshall, W.F., and Fung, J.C. (2019). Modeling meiotic chromosome pairing: a tug of war between telomere forces and a pairing-based Brownian ratchet leads to increased pairing fidelity. Phys Biol *16*, 046005. 10.1088/1478-3975/ab15a7.

70. Tarsounas, M., Morita, T., Pearlman, R.E., and Moens, P.B. (1999). Rad51 and Dmc1 Form Mixed Complexes Associated with Mouse Meiotic Chromosome Cores and Synaptonemal Complexes. J Cell Biology *147*, 207–220. 10.1083/jcb.147.2.207.

71. Slotman, J.A., Paul, M.W., Carofiglio, F., Gruiter, H.M. de, Vergroesen, T., Koornneef, L., Cappellen, W.A. van, Houtsmuller, A.B., and Baarends, W.M. (2020). Super-resolution imaging of RAD51 and DMC1 in DNA repair foci reveals dynamic distribution patterns in meiotic prophase. Plos Genet *16*, e1008595. 10.1371/journal.pgen.1008595.

72. Koornneef, L., Slotman, J.A., Sleddens-Linkels, E., Cappellen, W.A. van, Barchi, M., Tóth, A., Gribnau, J., Houtsmuller, A.B., and Baarends, W.M. (2022). Multi-color dSTORM microscopy in Hormad1-/- spermatocytes reveals alterations in meiotic recombination intermediates and synaptonemal complex structure. Plos Genet *18*, e1010046. 10.1371/journal.pgen.1010046.

73. Kim, K.P., Weiner, B.M., Zhang, L., Jordan, A., Dekker, J., and Kleckner, N. (2010). Sister Cohesion and Structural Axis Components Mediate Homolog Bias of Meiotic Recombination. Cell *143*, 924–937. 10.1016/j.cell.2010.11.015.

74. Xu, H., Beasley, M.D., Warren, W.D., Horst, G.T.J. van der, and McKay, M.J. (2005). Absence of Mouse REC8 Cohesin Promotes Synapsis of Sister Chromatids in Meiosis. Dev Cell *8*, 949–961. 10.1016/j.devcel.2005.03.018.

75. Reuter, M., Zelensky, A.N., Smal, I., Meijering, E., Cappellen, W.A. van, Gruiter, H.M. de, Belle, G.J. van, Royen, M.E. van, Houtsmuller, A.B., Essers, J., et al. (2014). BRCA2 diffuses as oligomeric clusters with RAD51 and changes mobility after DNA damage in live cells. J Cell Biology *207*, 599 613. 10.1083/jcb.201405014.

76. Paul, M.W., Sidhu, A., Liang, Y., Rossum-Fikkert, S.E. van, Odijk, H., Zelensky, A.N., Kanaar, R., and Wyman, C. (2021). Role of BRCA2 DNA-binding and C-terminal domain in its mobility and conformation in DNA repair. Elife *10*, e67926. 10.7554/elife.67926.

77. Zelensky, A.N., Schimmel, J., Kool, H., Kanaar, R., and Tijsterman, M. (2017). Inactivation of Pol θ and C-NHEJ eliminates off-target integration of exogenous DNA. Nature communications *8*, 66. 10.1038/s41467-017-00124-3.

78. Geissmann, Q. (2013). OpenCFU, a new free and open-source software to count cell colonies and other circular objects. Plos One *8*, e54072. 10.1371/journal.pone.0054072.

79. Peters, A.H.F.M., Plug, A.W., Vugt, M.J. van, and Boer, P. de (1997). SHORT COMMUNICATIONS A drying-down technique for the spreading of mammalian meiocytes from the male and female germline. Chromosome Res *5*, 66–68. 10.1023/a:1018445520117.

80. Koornneef, L., Paul, M.W., Houtsmuller, A.B., Baarends, W.M., and Slotman, J.A. (2023). Three-color dSTORM Imaging and Analysis of Recombination Foci in Mouse Spread Meiotic Nuclei. Bio-Protoc. *13*, e4780. 10.21769/bioprotoc.4780.

81. Alsheimer, M., and Benavente, R. (1996). Change of Karyoskeleton during Mammalian Spermatogenesis: Expression Pattern of Nuclear Lamin C2 and Its Regulation. Exp Cell Res *228*, 181–188. 10.1006/excr.1996.0315.

82. Winkel, K., Alsheimer, M., Öllinger, R., and Benavente, R. (2009). Protein SYCP2 provides a link between transverse filaments and lateral elements of mammalian synaptonemal complexes. Chromosoma *118*, 259–267. 10.1007/s00412-008-0194-0.

83. Essers, J., Hendriks, R.W., Wesoly, J., Beerens, C.E.M.T., Smit, B., Hoeijmakers, J.H.J., Wyman, C., Dronkert, M.L.G., and Kanaar, R. (2002). Analysis of mouse Rad54 expression and its implications for homologous recombination. Dna Repair *1*, 779–793. 10.1016/s1568-7864(02)00110-6.

84. Treuner, K., Findeisen, M., Strausfeld, U., and Knippers, R. (1999). Phosphorylation of Replication Protein A Middle Subunit (RPA32) Leads to a Disassembly of the RPA Heterotrimer*. J Biol Chem *274*, 15556–15561. 10.1074/jbc.274.22.15556.

85. Wojtasz, L., Daniel, K., Roig, I., Bolcun-Filas, E., Xu, H., Boonsanay, V., Eckmann, C.R., Cooke, H.J., Jasin, M., Keeney, S., et al. (2009). Mouse HORMAD1 and HORMAD2, two conserved meiotic chromosomal proteins, are depleted from synapsed chromosome axes with the help of TRIP13 AAA-ATPase. Plos Genet *5*, e1000702. 10.1371/journal.pgen.1000702.

86. Schindelin, J., Arganda-Carreras, I., Frise, E., Kaynig, V., Longair, M., Pietzsch, T., Preibisch, S., Rueden, C., Saalfeld, S., Schmid, B., et al. (2012). Fiji: an open-source platform for biological-image analysis. Nat Methods *9*, 676–682. 10.1038/nmeth.2019.

87. Modesti, M., Ristic, D., Heijden, T. van der, Dekker, C., Mameren, J. van, Peterman, E.J.G., Wuite, G.J.L., Kanaar, R., and Wyman, C. (2007). Fluorescent human RAD51 reveals multiple nucleation sites and filament segments tightly associated along a single DNA molecule. Structure *15*, 599 609. 10.1016/j.str.2007.04.003.

88. Ristic, D., Kanaar, R., and Wyman, C. (2011). Visualizing RAD51-mediated joint molecules: implications for recombination mechanism and the effect of sequence heterology. Nucleic Acids Res *39*, 155 167. 10.1093/nar/gkq766.

89. Holthausen, J.T., Loenhout, M.T.J. van, Sanchez, H., Ristic, D., Rossum-Fikkert, S.E. van, Modesti, M., Dekker, C., Kanaar, R., and Wyman, C. (2011). Effect of the BRCA2 CTRD domain on RAD51 filaments analyzed by an ensemble of single molecule techniques. Nucleic Acids Res *39*, 6558 6567. 10.1093/nar/gkr295.

90. Dümmler, A., Lawrence, A.-M., and Marco, A. de (2005). Simplified screening for the detection of soluble fusion constructs expressed in E. coli using a modular set of vectors. Microb Cell Fact *4*, 34. 10.1186/1475-2859-4-34.

91. RONG, M., MATSUDA, A., HIRAOKA, Y., and LEE, J. (2016). Meiotic cohesin subunits RAD21L and REC8 are positioned at distinct regions between lateral elements and transverse filaments in the synaptonemal complex of mouse spermatocytes. J Reprod Develop *62*, 623–630. 10.1262/jrd.2016-127.

92. Chan, Y.W., and West, S.C. (2018). A new class of ultrafine anaphase bridges generated by homologous recombination. Cell Cycle *17*, 2101–2109. 10.1080/15384101.2018.1515555.

93. Chan, Y.W., Fugger, K., and West, S.C. (2018). Unresolved recombination intermediates lead to ultra-fine anaphase bridges, chromosome breaks and aberrations. Nat Cell Biol *20*, 92–103. 10.1038/s41556-017-0011-1.

94. Chan, K.L., and Hickson, I.D. (2009). On the origins of ultra-fine anaphase bridges. Cell Cycle *8*, 3065–3066. 10.4161/cc.8.19.9513.

95. Davidson, I.F., and Peters, J.-M. (2021). Genome folding through loop extrusion by SMC complexes. Nat Rev Mol Cell Bio *22*, 445–464. 10.1038/s41580-021-00349-7.

96. Vries, F.A.T. de, Boer, E. de, Bosch, M. van den, Baarends, W.M., Ooms, M., Yuan, L., Liu, J.-G., Zeeland, A.A. van, Heyting, C., and Pastink, A. (2005). Mouse Sycp1 functions in synaptonemal complex assembly, meiotic recombination, and XY body formation. Gene Dev *19*, 1376–1389. 10.1101/gad.329705.

ACKNOWLEDGEMENTS

We would like to thank Dr Emmanuelle Martini and Dr Alberto Pendas for the helpful discussions of the model. This study was supported by the Oncode Institute, which is partly financed by the Dutch Cancer Society (KWF). We thank the Josephine Nefkens Cancer Program for infrastructure support. S.M. acknowledges funding by the Institut National de la Santé et de la Recherche Médicale (INSERM). S.M. and S.Z.J. were also supported by funding from the French Infrastructure for Integrated Structural Biology (ANR-10-INSB-05-01).

DATA AVAILABILITY

Raw microscopy images analyzed in the study have been deposited in BioStudies under accession S-BSST1203. Numerical data plotted in the figures is provided as a supplementary Excel file.

COMPETING INTERESTS

Authors declare no competing interests.

AUTHOR CONTRIBITIONS

Conceptualization: L.K., S.Z-J., R.K., W.B., and A.Z.; Methodology; L.K., A.M., and A.Z.; Software: L.K.; Investigation: L.K., S.vR-F., S.M. E.S-L., A.M., Y.vL., and J.E., Resources: A.M., and J.E.; Data analyses and interpretation; L.K., S.M., S. Z-J., M.B., R.K., W.B., and A.Z.; Visualization: L.K., W.B., and A.Z; Data curation: L.K., and A.Z.; Writing-Original Draft: L.K., W.B., and A.Z.; Writing-Review & Editing: all authors; Supervision: R.K., W.B., and A.Z.; Funding Acquisition: S.Z-J, R.K.

FIGURES

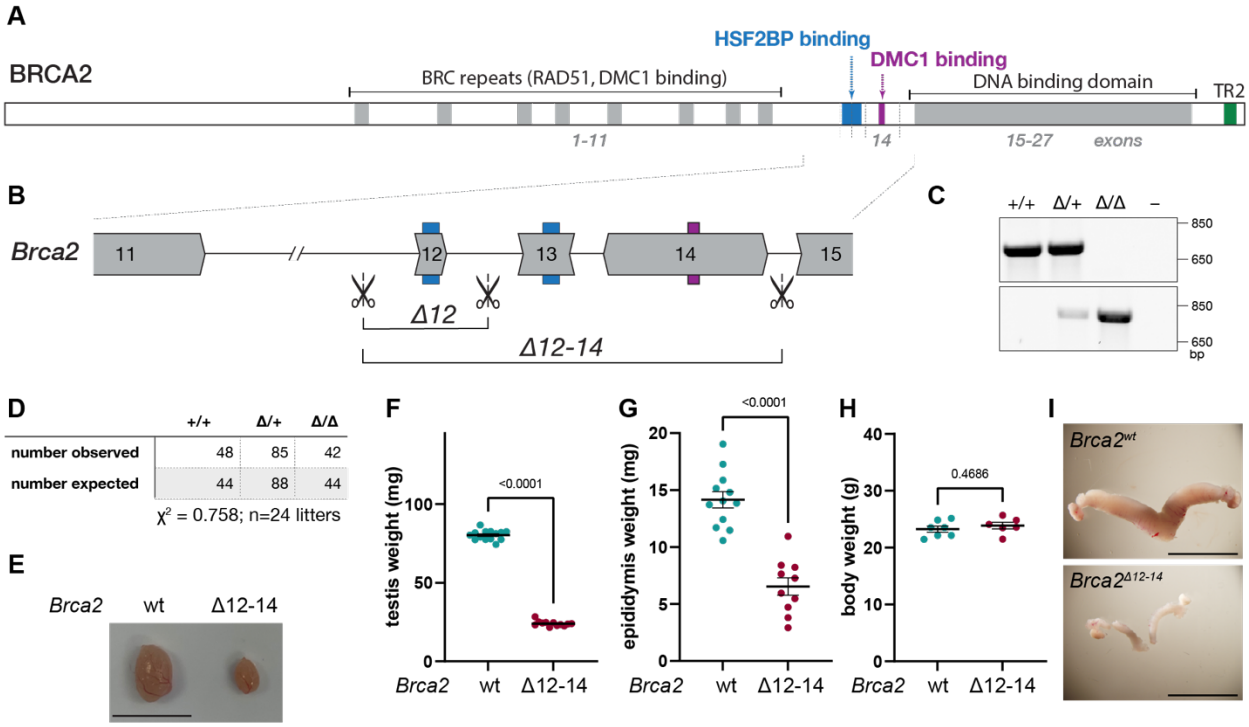

Figure 1. Characterization of *Brca2*$^{\Delta 12\text{-}14}$ mouse model. (**A**) Schematic domain structure of BRCA2 protein. (**B**) Exon-intron structure of the region targeted by CRISPR/Cas9 deletion. (**C**) RT-PCR and immunoblot analysis confirming the effect of exon 12-14 deletion on *Brca2* transcript and BRCA2 protein. (**D**) Numbers of pups born from intercrosses between *Brca2*$^{\Delta 12\text{-}14/+}$ animals and comparison to the numbers expected if Mendelian ratios are maintained. (**E**) Representative photographs of testes from *Brca2*^{wt} and *Brca2*$^{\Delta 12\text{-}14}$ littermate animals. Testis (**F**), epididymis (**G**) and body weight (**H**) in *Brca2*$^{\Delta 12\text{-}14}$ and control male mice (n=6-7, n=6-7 and n=5-6 respectively). All data is plotted, mean, s.e.m. and *p* values from two-tailed unpaired t-test are indicated. (**I**) Representative photographs of ovaries and uterus from *Brca2*^{wt} and *Brca2*$^{\Delta 12\text{-}14}$ littermate animals of 18 weeks old. Scale bar represents 1 cm (**E,I**).

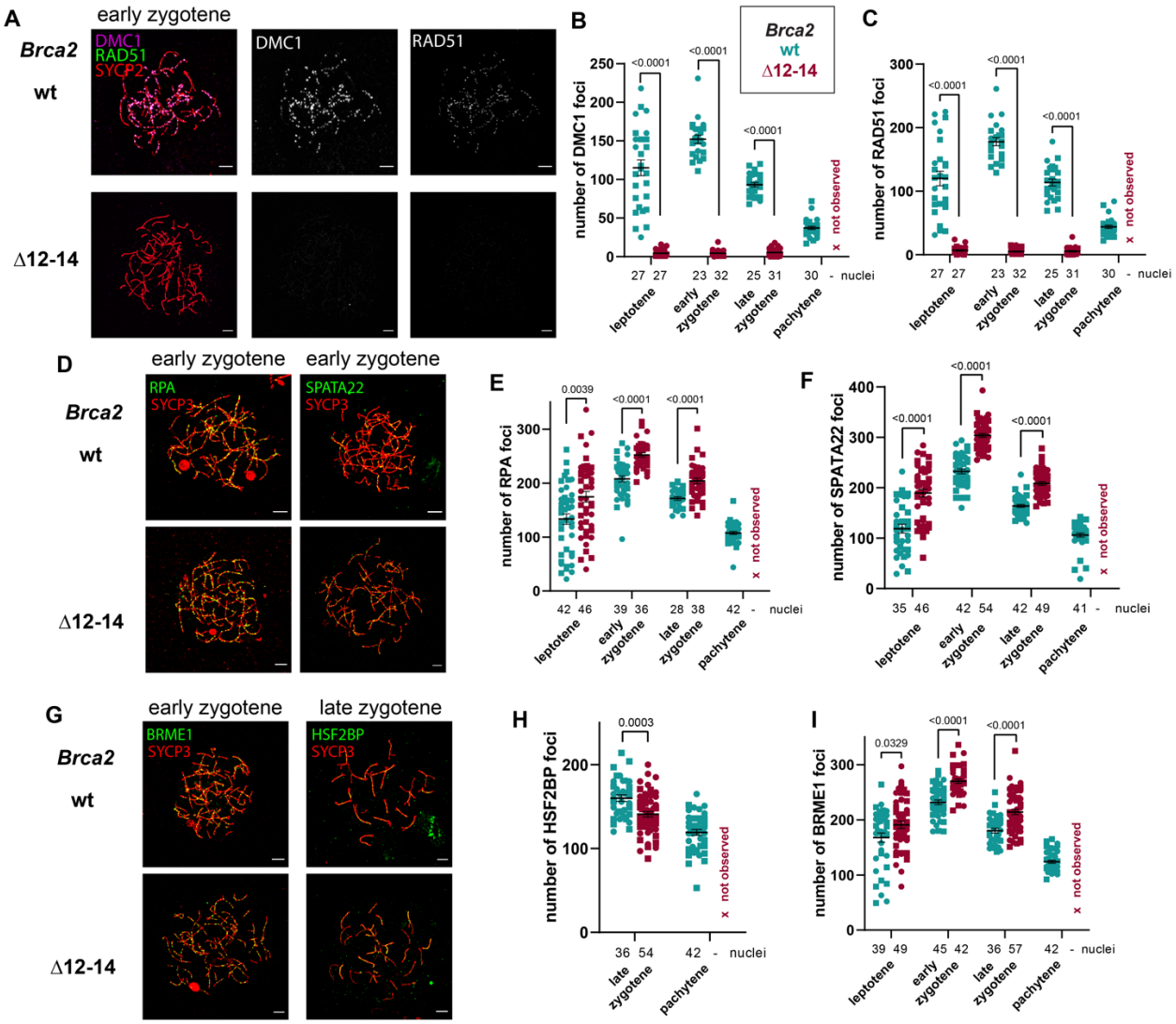

Figure 2. Meiotic analysis of *Brca2*$^{\Delta 12\text{-}14}$ spermatocytes. Immunofluorescent analysis of meiotic proteins on nuclear surface spread spermatocytes from *Brca2*$^{\Delta 12\text{-}14}$ and control mice. (**A**) Representative images of spread spermatocyte nuclei immunostained for RAD51 (green), DMC1 (magenta), and SYCP2 (red) including individual presentation of RAD51 or DMC1 in white. (**B**) Quantification of DMC1 foci. (**C**) Quantification of RAD51 foci. (**D**) Representative images of spread spermatocyte nuclei immunostained for RPA (green) or SPATA22 (green), and SYCP3 (red). (**E**) Quantification of RPA foci. (**F**) Quantification of SPATA22 foci. (**G**) Representative images of spread spermatocyte nuclei immunostained for BRME1 (green) or HSF2BP (green), and SYCP3 (red). (**H**) Quantification of HSF2BP foci. (**I**) Quantification of BRME1 foci. Mean, s.e.m., p-values from two-tailed unpaired t-test, and number of analyzed nuclei are indicated in the graphs. Symbol shapes represents individual animals: n = 2 for *Brca2*^{wt} and n= 2 for *Brca2*$^{\Delta 12\text{-}14}$. Sea blue color represents *Brca2*$^{+/+}$ and burgundy color represents *Brca2*$^{\Delta 12\text{-}14}$. For the mutant the pachytene stage was not observed. Scale bar represents 5 µm (**A,D,G**).

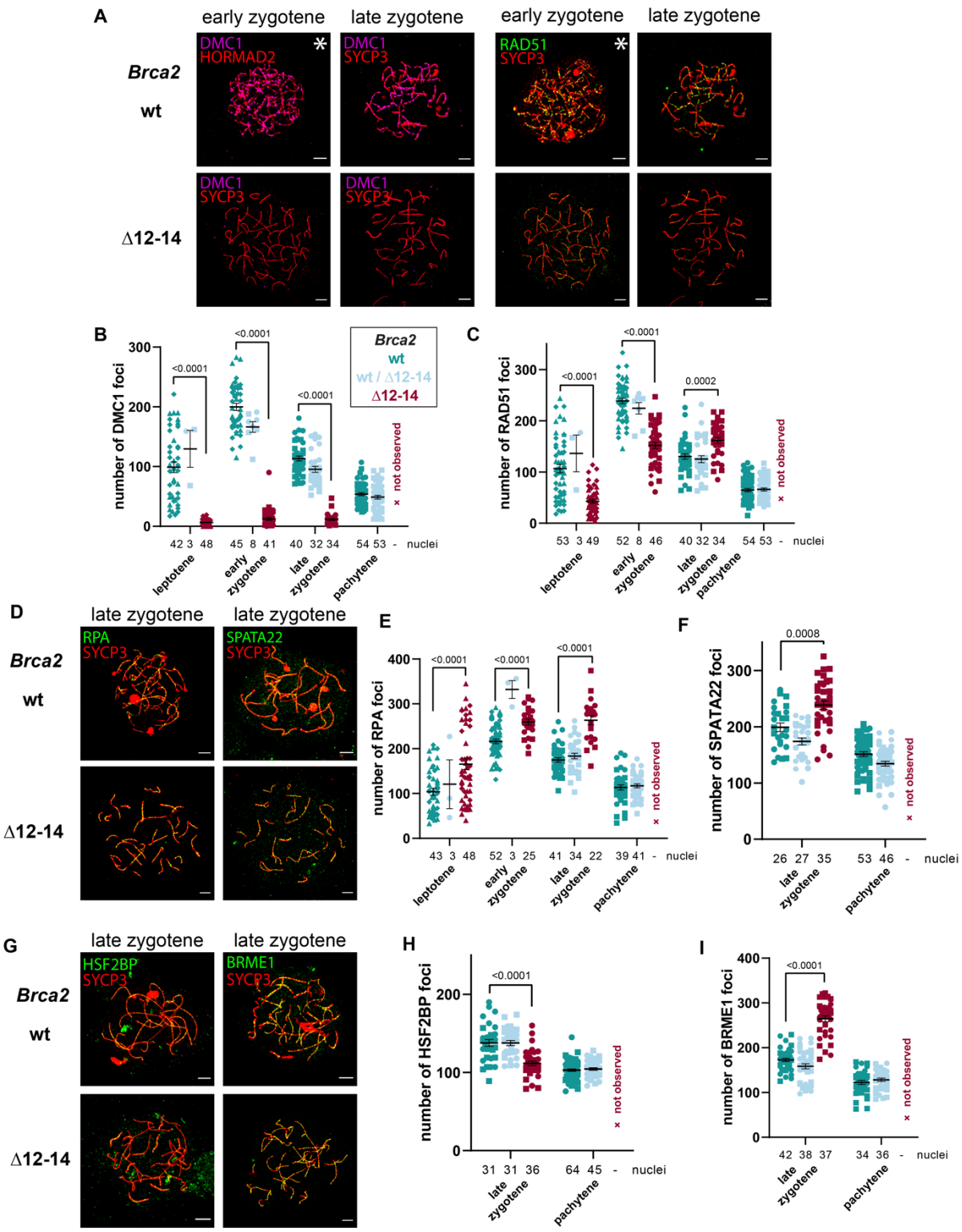

Figure 3. Meiotic analysis of *Brca2*$^{\Delta 12\text{-}14}$ oocytes. Immunofluorescent analysis of meiotic proteins on nuclear surface spread oocytes from E15.5 and E17.5 *Brca2*$^{\Delta 12\text{-}14}$ and control mice. (**A**) Representative images of spread spermatocyte nuclei immunostained for RAD51 (green) and DMC1 (magenta) with SYCP3 or HORMAD2 (red). Meiotic stage of nuclei is indicated above the images. For wild type late zygotene and pachytene and *Brca2*$^{\Delta 12\text{-}14}$ early zygotene and late zygotene, oocytes spreads of E17.5 mice were used. For the earlier stages (leptotene and early zygotene of wild type and leptotene of *Brca2*$^{\Delta 12\text{-}14}$) oocytes

spreads of E15.5 mice were used. Images from E15.5 spreads are indicated with an asterisks. (**B**) Quantification of DMC1 foci. (**C**) Quantification of RAD51 foci. (**D**) Representative images of spread oocyte nuclei immunostained for RPA (green) or SPATA22 (green), and SYCP3 (red). (**E**) Quantification of RPA foci. (**F**) Quantification of SPATA22 foci. (**G**) Representative images of spread oocyte nuclei immunostained for BRME1 (green) or HSF2BP (green), and SYCP3 (red). (**H**) Quantification of HSF2BP foci. (**I**) Quantification of BRME1 foci. Mean, s.e.m., p-values from two-tailed unpaired t-test, and number of analyzed nuclei are indicated in the graphs. Symbol shapes (circle, square, hexagon) represents individual E17.5 animals: n = 2 for *Brca2*^{wt}, n = 2 for *Brca2*$^{wt/\Delta 12\text{-}14}$ (n = 3 for SPATA22) and n = 2 for *Brca2*$^{\Delta 12\text{-}14}$. Data and images of E15.5 oocytes originate from 2 animals of *Brca2*^{wt} and 2 animals of *Brca2*$^{\Delta 12\text{-}14}$, which are represented in the graphs by the symbols rhombus and triangle. Sea blue color represents *Brca2*^{wt}, light blue color represents *Brca2*$^{wt/\Delta 12\text{-}14}$, burgundy color represents *Brca2*$^{\Delta 12\text{-}14}$. For the mutant the pachytene stage was not observed. Scale bar represents 5 µm (**A,D,G**).

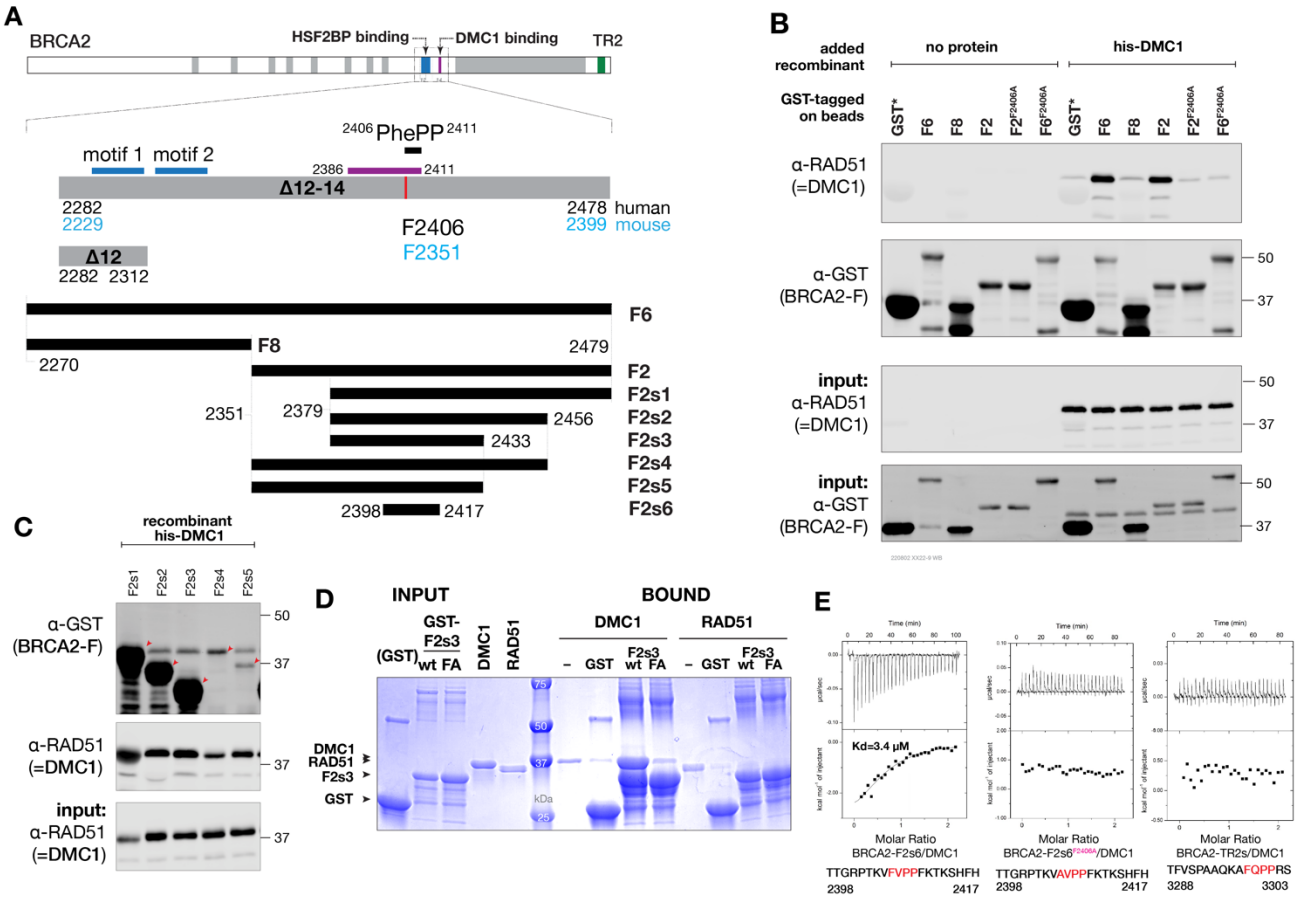

Figure 4. Biochemical characterization of the DMC1-BRCA2 interaction. (**A**) BRCA2 regions deleted in the mice (grey) and studied in pull-downs (black), HSF2BP-interacting motifs, PhePP motif and the peptide used in ref. [16] are indicated. Residue numbers for human BRCA2 are shown in black, mouse — in blue. (**B**) GST pull-down with the indicated GST-BRCA2 fragments immobilized on GSH-sepharose beads and used to precipitate recombinant his-DMC1. F2406A substitution variants fragments F2 and F6 predicted to disrupt the interaction with DMC1 were also tested. Proteins were detected by immunoblotting with anti-RAD51 antibody, which cross-reacts with DMC1, and anti-GST antibodies. GST* indicates GST-DCOH fusion protein produced after transformation with the original pETM-30 vector used for BRCA2 fragment cloning.[90] Experiment was performed twice with similar results. (**C**) GST pull-down assay with shortened variants of GST-tagged BRCA2 fragment F2 shown in panel A; replicate in Figure S5C. (**D**) Co-precipitation of purified recombinant untagged DMC1 and RAD51 with purified GST-tagged BRCA2 fragment F2s3 (wild type (wt) and F2406A variant (FA)) immobilized on the beads. Bound proteins were analyzed by SDS-PAGE and stained with Coomassie. (**E**) ITC analysis of the interaction between untagged DMC1 and synthetic peptides corresponding to BRCA2-F2s6 fragment, its F2406A variant, and the peptide from the RAD51-binding TR2 domain, containing a similar FxPP consensus. Experiments were performed twice with the same result: replica are shown in Figure S5D.

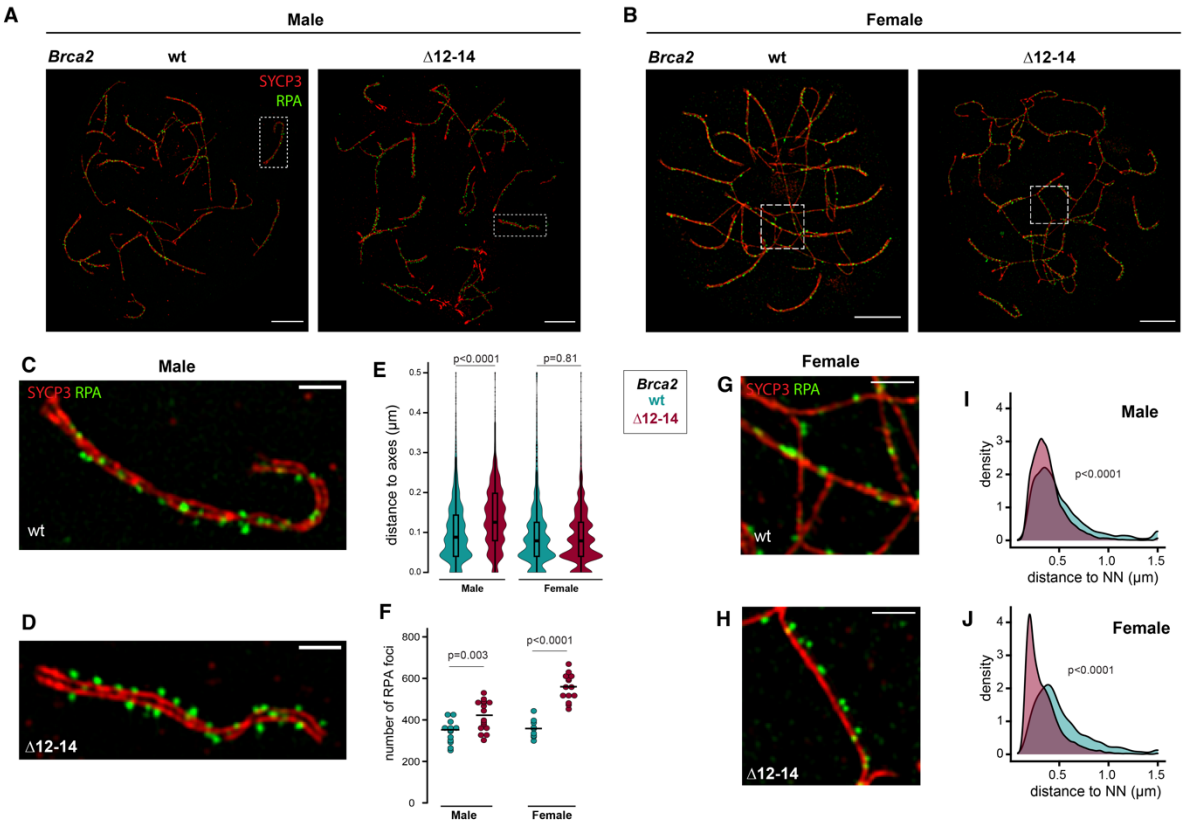

Figure 5. Super-resolution imaging analysis of RPA localization in meiocytes of *Brca2*$^{\Delta 12\text{-}14}$ mice. Structured illumination microscopy imaging of RPA (green) and SYCP3 (red) on nuclear surface spread spermatocytes (**A**) and oocytes (**B**) from wild type and *Brca2*$^{\Delta 12\text{-}14}$ mice. (**C, D**) Close-up of SIM image of RPA (green) and SYCP3 (red) on nuclear surface spread spermatocytes from wild type (**C**) and *Brca2*$^{\Delta 12\text{-}14}$ (**D**) spermatocytes to show the difference in RPA positioning relative to SYCP3. The whole nucleus is indicated in A. (**E**) Violin with boxplot of the shortest distance for each RPA focus to SYCP3 in wild type and *Brca2*$^{\Delta 12\text{-}14}$ spermatocytes and E17.5 oocytes at zygotene. Distances larger than 500 nm were plotted as 500 nm. (**F**) Quantification of the number of RPA foci at zygotene nuclei for male and female *Brca2*$^{\Delta 12\text{-}14}$ and control mice. Close-up of SIM image of wild type (**G**) and *Brca2*$^{\Delta 12\text{-}14}$ (**H**) E17.5 oocytes to show the difference in paired RPA foci. The whole nucleus is indicated in B. Density plot of the distance to the nearest neighbor RPA focus of male (**I**) and female (**J**) *Brca2*$^{\Delta 12\text{-}14}$ and control mice to show an increase in close-positioned paired RPA foci in *Brca2*$^{\Delta 12\text{-}14}$ oocytes. Nearest neighbor distances larger than 1500 nm were plotted as 1500 nm. Scale bar represents 5 µm (**A,B**), 2 µm (**K**) and 1 µm (**C,D,G,H**). Statistical significance (p-values) using a Wilcoxon test (**E**), two-tailed unpaired t-test (**F**) or Kolmogorov–Smirnov test (**I,J**) are indicated in the figures.

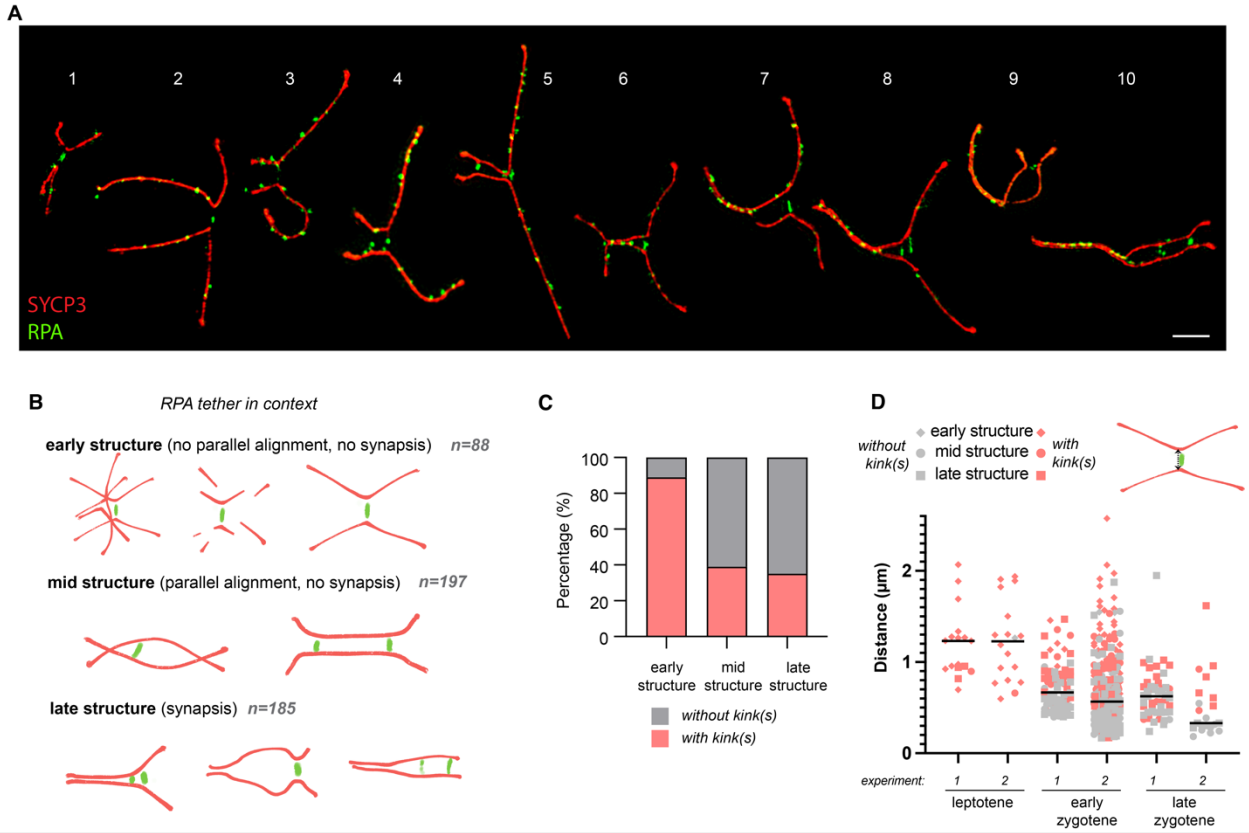

Figure 6. RPA tether foci identified by SIM imaging. (**A**) Compilation of examples of the RPA tethers observed in SIM (RPA is green, SYCP3 is red) data from wild type spermatocytes. These structures are not observed in *Brca2*$^{\Delta 12\text{-}14}$ spermatocytes. For the purpose of visualization, images of the chromosome pairs were isolated from the different images of nuclei and pasted together in this combined image. (**B**) Several cartoons of possibilities of the different contexts where RPA tethers are present: early (no alignment, no synapsis), mid (alignment, no synapsis) and late structures (synapsis) including the number of RPA tethers in those categories observed in 73 wild type nuclei. (**C**) Quantification of the presence (light red) or absence (grey) of kinks in the chromosomal axes around the RPA tether in the different contexts of the RPA tether. (**D**) Quantification of the distance between the two points on the chromosomal axes to which the line defined by the RPA tether projects per meiotic stage. The presence (light red) or absence (grey) of kinks is indicated. The different structures are indicated by the shape of the points (triangle represents early structure, circle represents mid structure, square represents late structure). Data from two independent experiments is plotted.

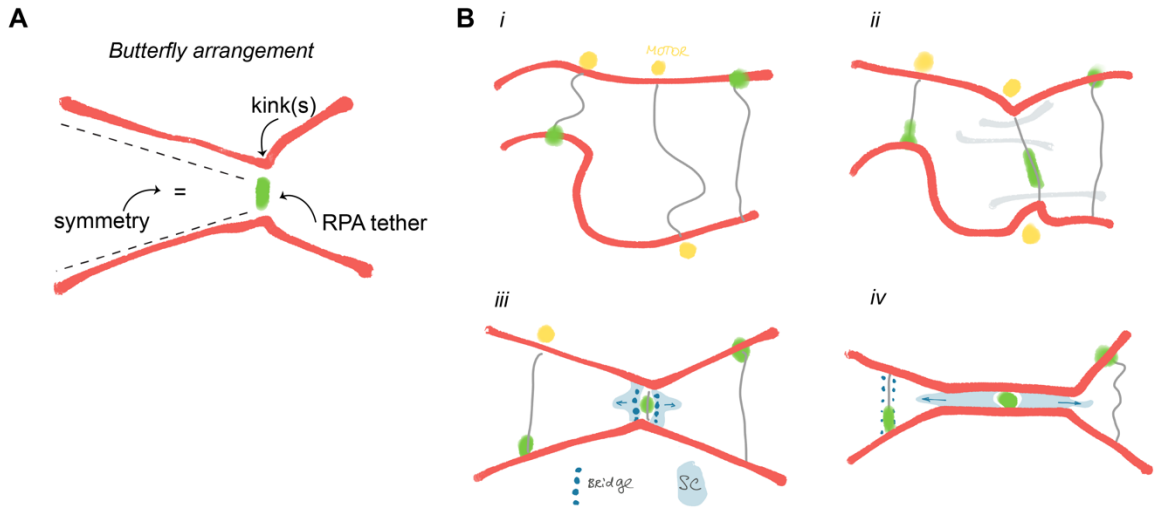

Figure 7. Tensioned DNA tether model. (**A**) Key features found in the butterfly arrangement. (**B**) The tensioned DNA tether model of homologous synapsis. Grey lines indicate DNA connections between homologs, yellow circles indicate the hypothesized molecular motors that reduce the length of the DNA tethers bringing homologs closer together (step *i*). Occasionally, clashes with other chromosomes (light grey, step *ii*) create counter force sufficient to induce mechanical tension that results in the elongated RPA tethers and kinks in the axial element. As the homologs come closer together at one or multiple points, proteinaceous connections (bridges and eventually synapsis) can form, stabilizing the interaction (step *iii*). Once initiated, synapsis rapidly progresses, while continued shortening of the tethers can facilitate bringing together unsynapsed regions (step *iv*).

SUPPLEMENTARY FIGURES

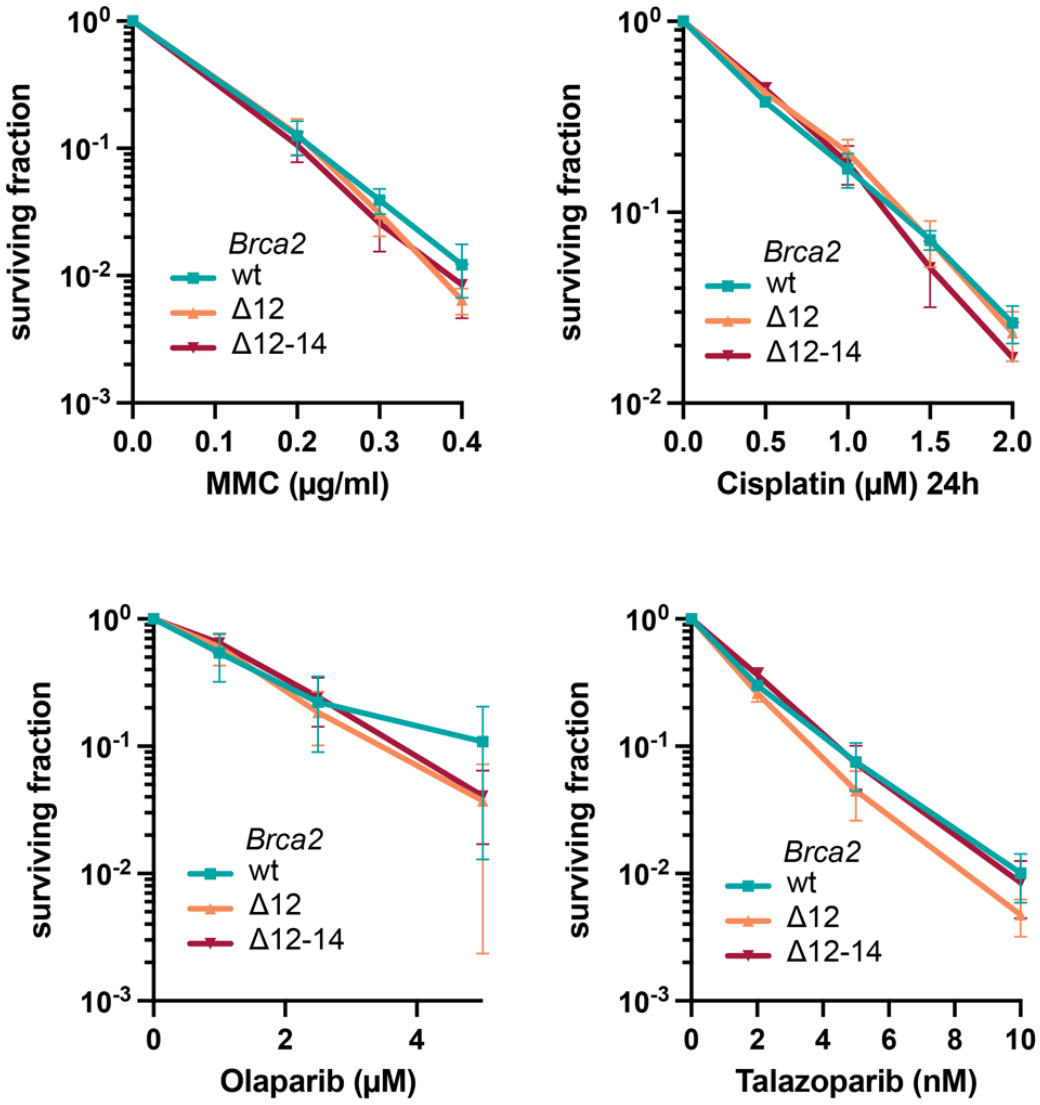

Supplementary Figure S1. Clonogenic survivals of wild type, *Brca2*$^{\Delta 12}$ and *Brca2*$^{\Delta 12\text{-}14}$ mES cells.

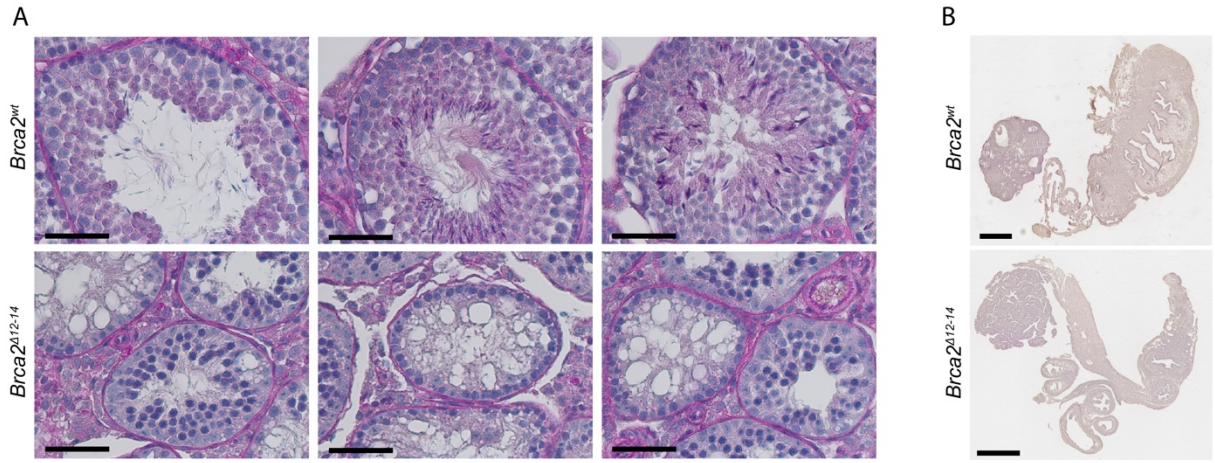

Supplementary Figure S2. Testis and ovary histology. (**A**) Representative histological images of PAS-staining on testis cross-sections of wild type and *Brca2*$^{\Delta 12\text{-}14}$ mice. (**B**) Representative histological images of HE-staining on ovary cross-sections of wild type and *Brca2*$^{\Delta 12\text{-}14}$ mice (18 weeks old). Scale bar represents 50 µm (**A**) and 500 µm (**B**).

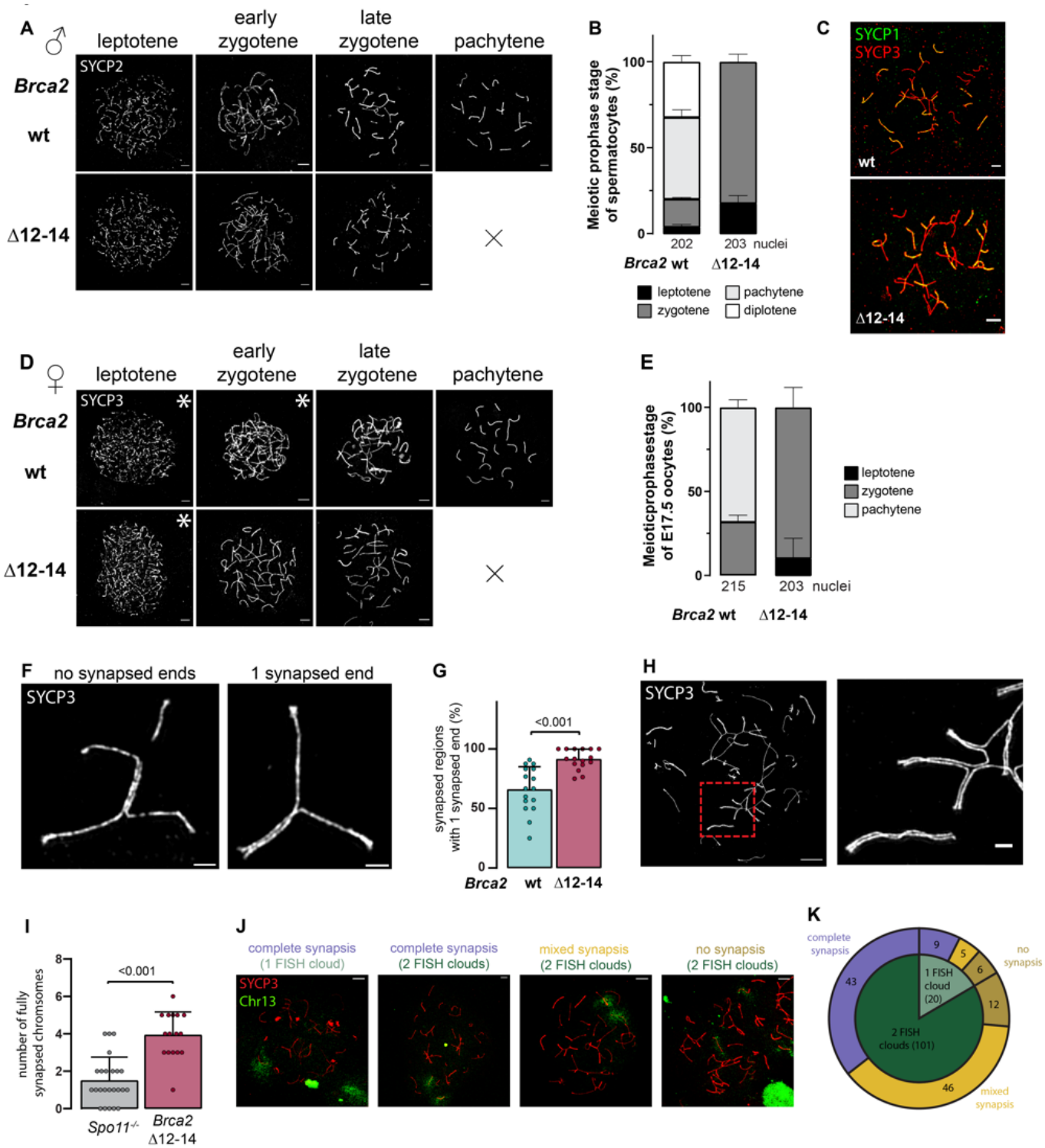

Supplementary Figure S3. Extended meiotic analysis of synapsis in *Brca2*$^{\Delta 12\text{-}14}$ meiocytes. (**A**) Immunostaining for SYCP2 on different meiotic stages of spermatocytes of *Brca2*$^{\Delta 12\text{-}14}$ and control mice. (**B**) Quantification of meiotic stages of spread nuclei of spermatocytes of *Brca2*$^{\Delta 12\text{-}14}$ and control mice. (**C**) Representative images of spread spermatocyte (wild type and *Brca2*$^{\Delta 12\text{-}14}$) nuclei immunostained for SYCP1 (green) and SYCP3 (red). (**D**) Immunostaining for SYCP3 on different meiotic stages of E15.5 and E17.5 oocytes of *Brca2*$^{\Delta 12\text{-}14}$ and control mice. Images from E15.5 oocytes are indicated with an asterisk. (**E**) Quantification of meiotic stages of spread nuclei of E17.5 oocytes of *Brca2*$^{\Delta 12\text{-}14}$ and control mice. Mutant meiocytes lack the pachytene-stage. (**F**) SIM image of a synapsed chromosomal axes in a zygotene wild type spermatocyte immunostained for SYCP3 showing with no

synapsed ends (left) and 1 synapsed end (right). (**G**) Bar plot of frequency of synapsed regions in wild type and *Brca2*$^{\Delta 12\text{-}14}$ spermatocytes with 1 synapsed end (fully synapsed chromosomes were excluded). **(H**) SIM image of a whole (left) and zoomed-in (right) late zygotene *Brca2*$^{\Delta 12\text{-}14}$ nuclear surface spread spermatocyte immunostained for SYCP3 showing complete and non-homologous synapsis. (**I**) Bar plot of number of fully synapsed chromosomes determined on super-resolution microscopy images of *Spo11*$^{-/-}$ and *Brca2*$^{\Delta 12\text{-}14}$ zygotene spermatocytes. (**J**) Examples of spread zygotene spermatocytes of *Brca2*$^{\Delta 12\text{-}14}$ and control mice immunostained for SYCP3 (red) and combined with fluorescent in situ hybridization of probe for chromosome 13 (green) whereby fully synapsed chromosomes, or chromosomes with mixed synapsis or no synapsis chromosomes were detected and scored for the presence of one or two FISH signals on these structures. (**K**) Quantification of different situations indicated in panel J on 121 spread zygotene *Brca2*$^{\Delta 12\text{-}14}$ spermatocytes of two different animals in a pie chart. Scale bars represent 5 µm (**A,D, H large, J**) or 1 µm (**F, H small**).

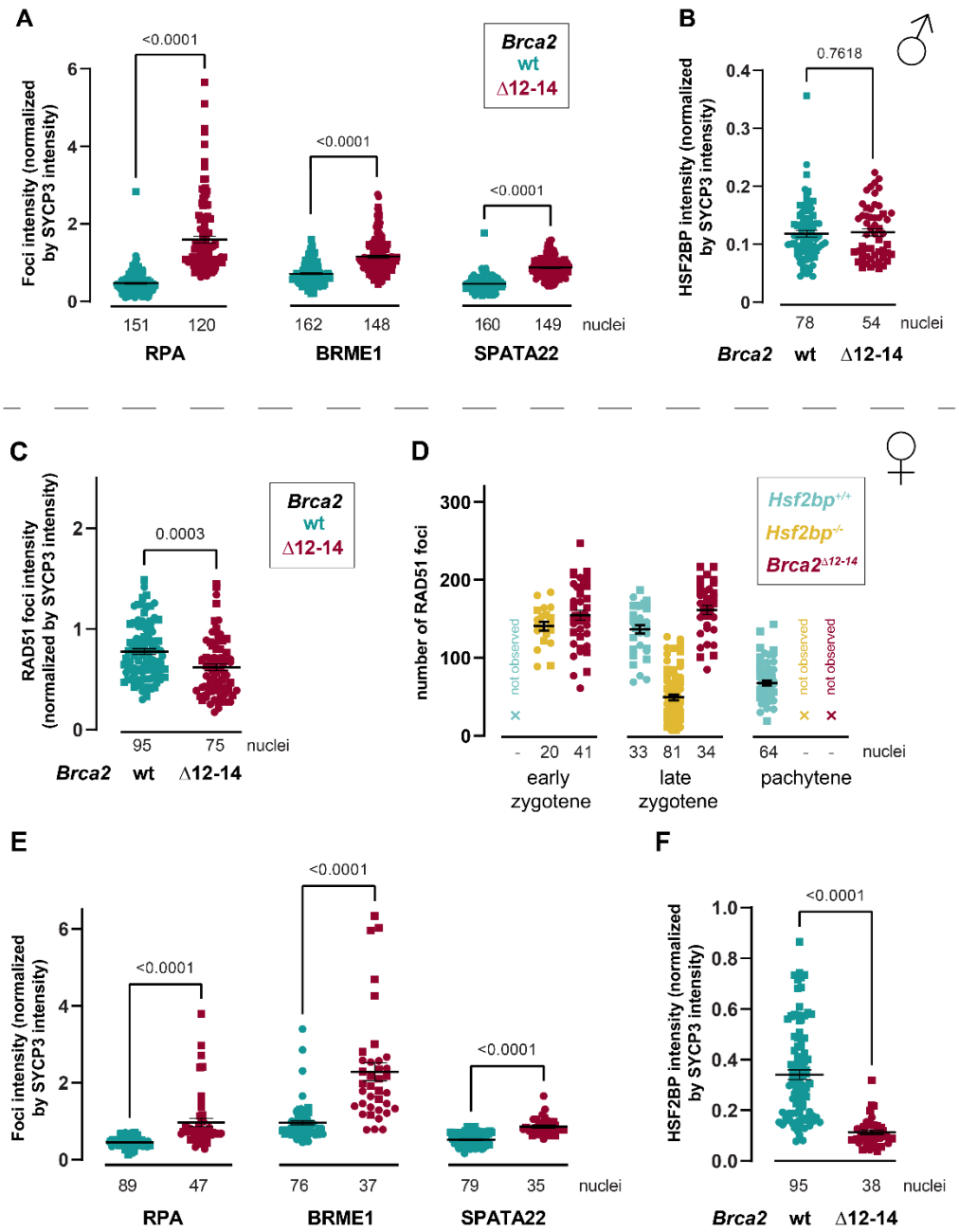

Supplementary Figure S4. Extended meiotic foci analysis of *Brca2*$^{\Delta 12\text{-}14}$ meiocytes. Quantification of RPA, BRME1 and SPATA22 foci intensity in spermatocytes (**A**) and E17.5 oocytes (**E**) of *Brca2*$^{\Delta 12\text{-}14}$ and control mice. **(B)** Quantification of HSF2BP intensity in spermatocytes (**B**) and E17.5 oocytes (**F**) of *Brca2*$^{\Delta 12\text{-}14}$ and control mice. All intensity quantifications (C-D) were normalized by SYCP3 intensity. Mean, s.e.m., p-values from two-tailed unpaired t-test, and number of analyzed nuclei are indicated in the graphs. Symbol shapes represent individual animals. Number of analyzed nuclei is indicated in the graph pooled from 2 animals per genotype. **(C)** Quantification of RAD51 foci intensity in E17.5 oocytes of *Brca2*$^{\Delta 12\text{-}14}$ and control mice. **(D)** Quantification of RAD51 foci number on *Hsf2bp*$^{+/+}$, *Hsf2bp*$^{-/-}$ and, *Brca2*$^{\Delta 12\text{-}14}$ E17.5 oocyte spreads (*Brca2*$^{\Delta 12\text{-}14}$ quantification is the same as in Figure 3C). All intensity quantifications (**A-C, E-F**) were normalized by SYCP3 intensity. Mean, s.e.m., p-values from two-tailed unpaired t-test, and number of analyzed nuclei are indicated in the graphs. Symbol shapes represent individual animals. Number of analyzed nuclei is indicated in the graph pooled from 2 animals per genotype. Sea blue color represents *Brca2*$^{+/+}$ and burgundy color represents *Brca2*$^{\Delta 12\text{-}14}$. Light sea blue and ocher yellow color represent *Hsf2bp*$^{+/+}$ and *Hsf2bp*$^{-/-}$ respectively. For the mutants the pachytene stage was not observed, and the early zygotene stage was not observed in E17.5 *Hsf2bp*$^{+/+}$ oocytes.

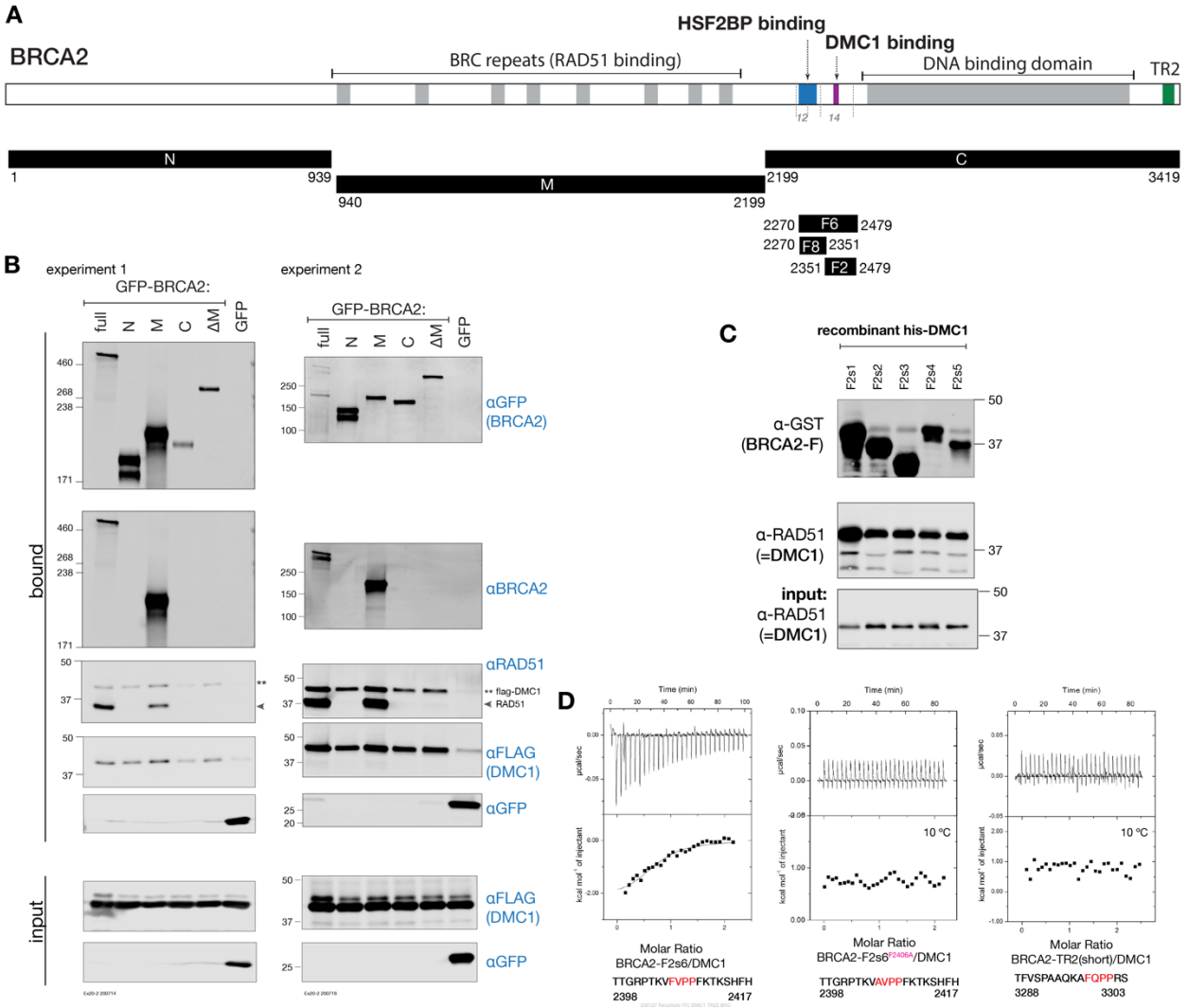

Supplementary Figure S5 (related to Figure 4). (**A**) BRCA2 protein scheme showing the fragments used to map the DMC1 interaction domain. (**B**) Immunoprecipitation with anti-GFP nanobody beads from HEK293T cells co-overproducing GFP-BRCA2 fragments and Flag-DMC1. Bound and input proteins were detected by immunoblot with the indicated antibodies. Endogenous RAD51 was detected with antibody, which also cross-reacts with DMC1. These attempts to use the same approach as we previously used to map the HSF2BP-BRCA2 interaction were inconclusive due to the propensity of DMC1 to co-precipitate equally efficiently with all BRCA2 fragments we tested. (**C**) Repeat of the GST pull-down experiments shown in Figure 4C. (**D**) Repeat of the ITC experiment shown in Figure 4E.

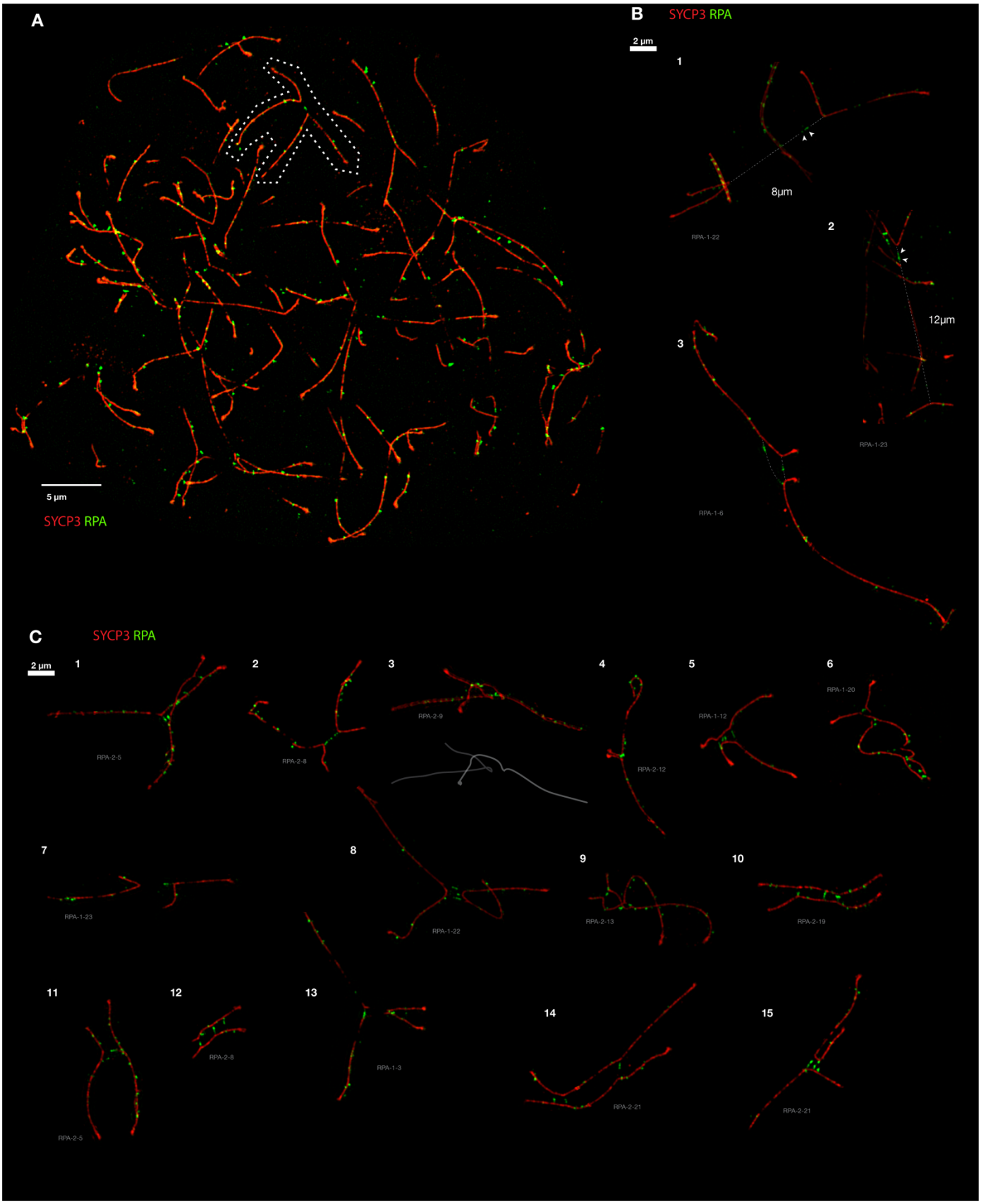
A
5 µm
SYCP3 RPA
B
SYCP3 RPA
2 µm
1
8µm
RPA-1-22
2
12µm
RPA-1-23
3
RPA-1-6
C
SYCP3 RPA
2 µm
1
RPA-2-5
2
RPA-2-8
3
RPA-2-9
4
RPA-2-12
5
RPA-1-12
6
RPA-1-20
7
RPA-1-23
8
RPA-1-22
9
RPA-2-13
10
RPA-2-19
11
RPA-2-5
12
RPA-2-8
13
RPA-1-3
14
RPA-2-21
15
RPA-2-21

1

Supplementary Figure S6 (related to Figure 5). Extended galleries of RPA tethers in the spermatocyte SIM data. (**A**) Illustration of the cropping mask applied to isolate chromosomes linked by RPA tethers for analysis and to produce galleries shown in Figure 5K and panels B and C. The dotted white outline indicates the structure Figure 5K, #2. (**B**) Examples of three structures with exceptionally long RPA tethers that could still be traced. White dotted lines indicate the inferred connections, length is indicated. Image of origin is indicated. (**C**) Extended gallery of RPA tethers. Scale bar = 2 µm.

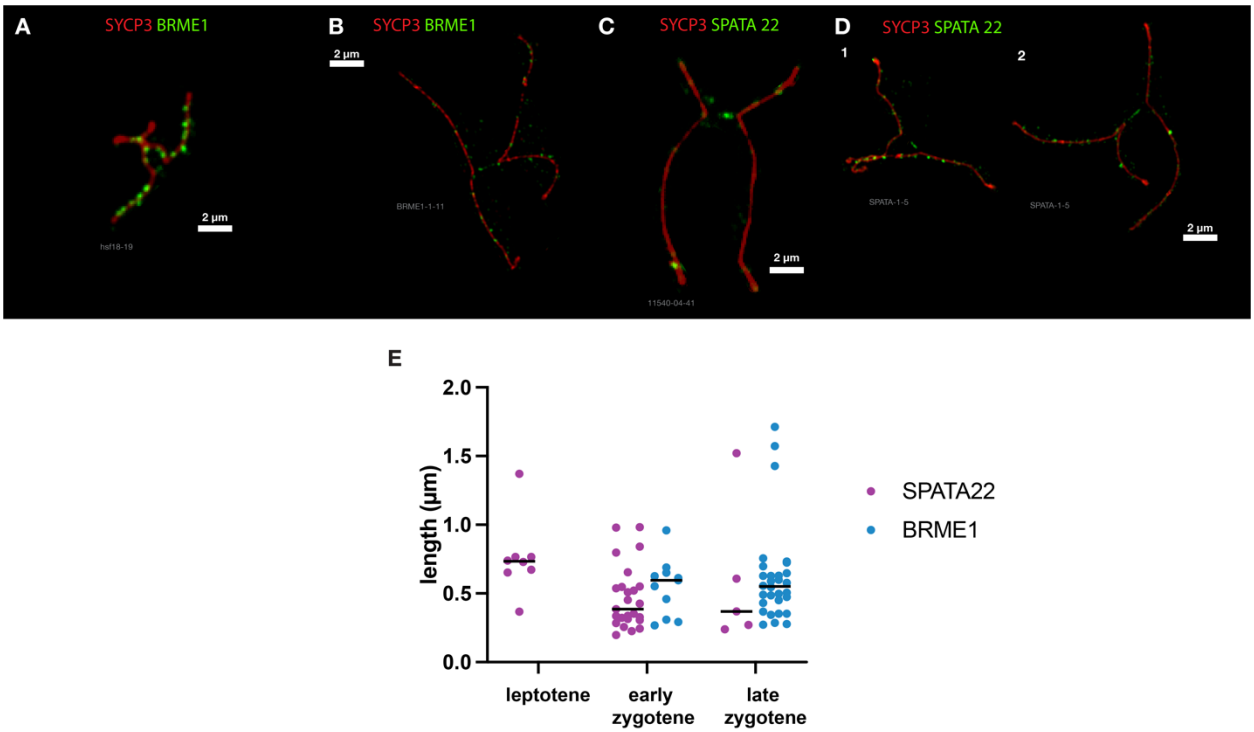

Supplementary Figure S7 (related to Figure 5). Localization of SPATA22 and BRME1 to tensioned DNA tethers in spermatocytes. (**A**) A single example of chromosomes in butterfly arrangement connected by a tether marked with BRME1 we found in the confocal microscopy images analyzed in Figure 2I. (**B**) Examples of BRME1 on a "butterfly" structure in the SIM dataset. (**C**) Example of SPATA22-decorated tether in confocal dataset analyzed in Figure 2F. (**D**) Examples of SPATA22-decorated tether in the SIM dataset. Structure 2 is the only example of non-symmetrical butterfly we observed. (**E**) Tether lengths in SPATA22 and BRME1 SIM images. All data points and median are plotted. The experiment was performed once.

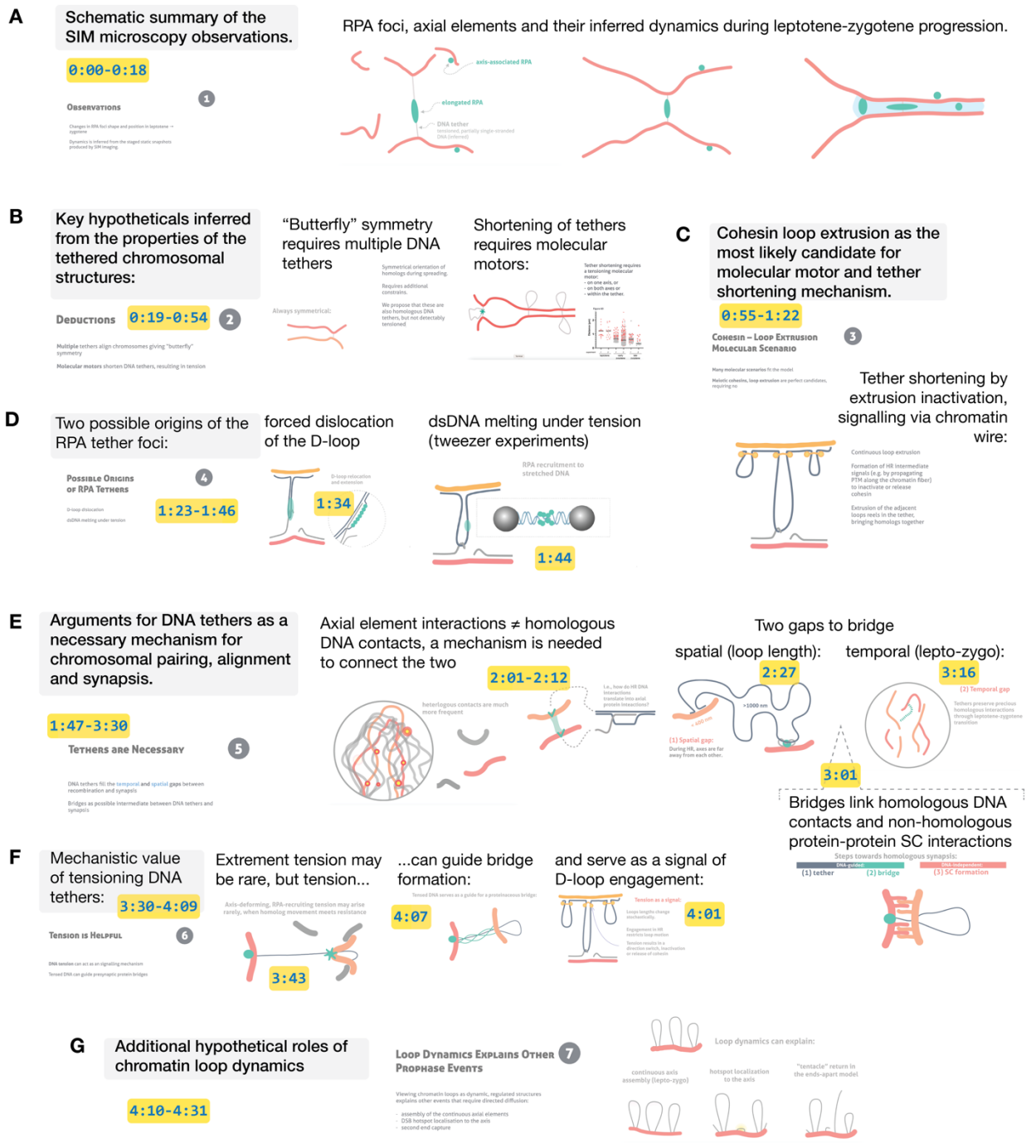

Supplementary Figure S8. Supplementary movie annotation. Supplementary movie illustrates in a form of animation the main components of the model described in the main and the supplementary extended discussions. Panels (**A-G**) correspond to the 7 parts of the movie, with key points and screenshots of the animations. Yellow labels give references to the timestamps (min:sec).

SUPPLEMENTARY EXTENDED DISCUSSION

Is Brca2$^{\Delta 12\text{-}14}$ phenotype a compound copy of Hsf2bp and Dmc1 disruption?

Our hypothesis that *Brca2*$^{\Delta 12\text{-}14}$ phenotype is a compound of the *Hsf2pb*$^{-/-}$ and *Dmc1*$^{-/-}$ phenotypes has two caveats. First, it assumes that the HSF2BP-BRCA2 interaction is essential in meiosis rather than in some other physiological context. While highly plausible, this assumption was challenged by the lack of a pronounced meiotic phenotype in our *Brca2*$^{\Delta 12}$ model [21]. Second, in *Brca2*$^{\Delta 12\text{-}14}$ spermatocytes the recombinase foci are completely abolished, while in *Hsf2bp*$^{-/-}$ spermatocytes some residual foci were observed [18,20]. Thus, we have to assume that either the deleted region has some additional effect on RAD51 loading or stability in spermatocytes but not in oocytes, or that RAD51 recruitment is dependent on DMC1 in spermatocytes but not oocytes, although the latter appears not to be the case based on *Dmc1* knock-out phenotypes [31,32]. Mouse models where the DMC1- and HSF2BP-binding domains of BRCA2 are removed separately or a double knockout of *Dmc1* and *Hsf2bp* are required to resolve these questions.

In addition, the earlier proposed role for HSF2BP as meiotic localizer of BRCA2 [19] does not apply in female meiotic HR, since RAD51 can be loaded (by BRCA2) in the absence of HSF2BP-BRCA2 interaction as shown in Figure 3. Also, HSF2BP foci numbers were reduced, while BRME1 foci number and intensity increased in *Brca2*$^{\Delta 12\text{-}14}$ meiocytes. This shows that both HSF2BP and BRME1 are still capable of associating with DSB sites if the HSF2BP-binding domain of *Brca2* is deleted, but also indicates that the proteins may not always colocalize.

RPA tethers in relation to meiotic bridges

Structures similar to RPA tethers in context of a late structure have been observed by others in different organisms, and were termed zygotene or transformed nodules, interaxis bridges or bridge-like structures [39,41,56,58,67] and proposed to act as starting points of SC formation and/or play a role in homology search [39,41,67]. In mouse, it has been reported that RPA [41], RAD51/DMC1 [70] and recently also cohesin protein RAD21L [91] bind to these bridges. Localization of RPA in such bridges, or in between more closely aligned or synapsed axial/lateral elements has been proposed to represent D-loops [67]. Based on the observed tension between the tethers, and the very elongated shape of some of the tethers, we propose an additional possible RPA recruitment mechanism, in analogy to the binding of RPA to dsDNA under tension in anaphase bridges and to DNA that is experimentally brought under tension by the use of optical tweezers [60,61]. We hypothesize that dsDNA is (also) present in the tethers, and will melt when over-stretched, resulting in ssDNA-like regions that will (also) be coated with RPA [8]. We hypothesize that the known movements of telomeric ends of the chromosomal axes along the nuclear envelope, in combination with possible entanglements may occasionally generate enough tension to melt the dsDNA leading to the occasional observation of elongated RPA tethers between kinked lateral elements. We further propose that molecular forces sufficient to achieve such tension can be created in a manner similar to the tensed DNA strands that are observed during late stages of mitosis if chromosomes moving to the opposite poles remain connected by DNA due to mishaps during or after the replication [9–12]. However, the tethers are thought to be the result of (post) strand invasion events that involve recognition of significant stretches of homologous DNA, and these structures also involve base-pairing. Thus, the

model needs to include the proposition that these HR intermediates would have to be protected from the tension, to ensure their stability.

Possible molecular scenarios for the tensioned DNA tethers model

Our model is compatible with multiple molecular scenarios and their combinations (Table 1). RPA may be recruited to the tether directly due to tension-induced DNA conformation change or represent a conventional HR intermediate, e.g. a D-loop within a recombinosome that dissociated from the axial element due to tension, or both. The main question is the nature of the molecular motor creating the tension and its localization within the tether. The most likely motor candidates are proteins that can translocate along dsDNA, anchored at the axial element. But HR intermediate remodeling (e.g. by branch migration) within the tether can also affect the length of the tether.

RPA origin:	Source of Tension:	Homology Recognition time	Homology Recognition configuration
RPA-R (3'-overhang)	spreading	pre-zygotene (fragmented or forming AE)	DSB ends together at axial element
RPA-D (D-loop)	chromosome movement	zygotene (continuous AE)	DSB ends separate (tentacle)
RPA-T (tensioned DNA)	D-loop processing		
	cohesin + loop extrusion		
	other (translocase)		

Table 1. Multiple molecular scenarios and their combinations. Different options for the origin of the RPA tether, the source of the tension, and timing and configuration of homology recognition. We favor the grey combination(s).

Detailed description of the scenario involving cohesin as motor

This specific scenario is inspired by two sets of observations in somatic cells: the properties of overstretched DNA and the chromatin loop extrusion model of gene expression regulation in interphase nucleus and chromosome compaction in G2.

First, as has been demonstrated in vitro using optical tweezer experiments, dsDNA will melt when over-stretched, resulting in ssDNA regions that become coated with RPA, if it is added to the reaction [61]. Whether molecular forces sufficient to achieve such tension can be created within the nucleus is not clear, but tensed DNA strands are observed during late stages of mitosis if chromosomes moving to the opposite poles remain connected by DNA due to mishaps during or after the replication [62,92–94]. Such mitotic DNA tethers are referred to as anaphase bridges, appear tensed, are also coated with RPA, and dsDNA melting under tension is one of the proposed mechanisms for RPA localization.

Second, organization of chromatin into loops is viewed a major mechanism of gene expression regulation in interphase cells [95]. The loops are viewed as dynamic structures that are organized and adjusted by the SMC family proteins. Viewing SMC proteins (cohesin and condensin) as active translocases rather than merely topological clamps, helps not only to explain how distant enhancers (dynamically) affect their

targets, but also how chromosome structure forms during transition to mitosis. Since meiotic cohesins REC8 and RAD21L are the key component of axial elements, they are good candidates for the role of the motor.

Combining these notions with the elements of the most accepted models of meiotic HR, we propose the following sequence of events.

1. For the scenario we choose the following starting configuration:
   - DSB has been induced, the recombinosome is anchored in the axial element that is not yet completely formed (leptotene).
   - Both ends of the DSB are located within the recombinosome.
   - The homologous sequence in the homologous chromosome is in a chromatin loop, not anchored in the axial element, at a potentially substantial distance from it.
2. Chromosomal rearrangements and bouquet movements increase the probability of the recombinosome coming in contact with the homologous sequence in the loop of the homologue. They also create a lot of non-specific short-lived encounters between the axial elements that will have a very small chance of leading to (heterologous) synapsis initiation, and this will be dynamic and reversible except in certain mutant situations, when homologous synapsis is not possible.
3. Upon probing the homologous chromatin loop, one of the DSB ends in the recombinosome invades the homolog, resulting in single-end invasion. There is no known mechanism to specifically stop the movement of the region now involved in the precious homologous interaction, and they can drift apart. The corresponding axial elements will be too far away for synapsis initiation and alignment is not yet established.
4. The strand invasion intermediate is stabilized within the recombinosome, establishing the stable DNA connection between the two homologs. The length of the connection is in the order of, and proportional to, the average length of chromatin loops.
5. The previous step happens for multiple DSBs per pair of homologs. Multiple tethers enable distant alignment between the homologs.
6. The connecting DNA loop is reeled in, pulling the chromosome together.
   - This transition to reeling in can happen globally or be triggered by some mechanism that senses the formation of the strand invasion intermediate (e.g. involving tension or chromatin modification)
   - This happens gradually for the multiple contacts between the homologues.
7. Depending on how much resistance the homologs that are being pulled together experience from the nucleoplasm, from the encounters with other chromosomes, and from DNA entanglements, the pulling force can get strong enough to induce deformation of the axial elements (kinks), local melting of the DNA within the tether, which attracts RPA, and partial dislocation of the recombinosome from the axial element. This whole process may be dynamic, and even reverse, in the chaotic early stages when multiple entanglements are likely to occur and prevent proper alignment. However, if chromosomal movement meets no resistance there is no melting, kinking or (additional) RPA recruitment.
8. Once the first regions approach each other to a distance of around 400-200nm (based on the distance between aligned axial elements in the *Sycp1* knockout [96]), synapsis is induced and propagates rapidly. Reeling in of the DNA connection also continues and helps to bring distal regions closer together.

9. Up to this point, multiple tethers have been required for proper pairing and end-to end alignment in the previous steps. Now they have served their purpose. Most of the HR intermediates can be resolved without crossover.